March 2007

ISSN 1211—877X

CZECH AEROSPACE *Proceedings*

LETECKÝ *zpravodaj*

In this issue:

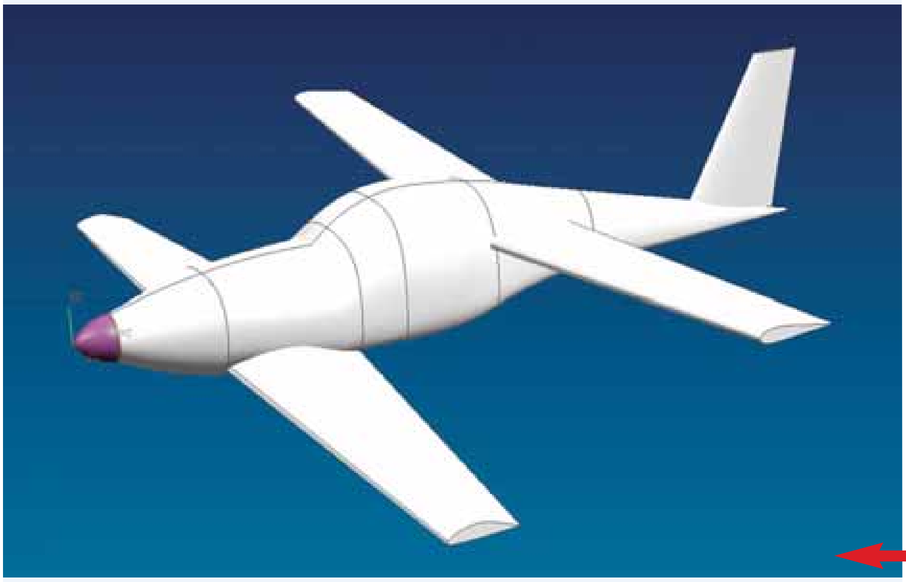

Foto Jan Kouba

No. 1 / 2007

CZECH AEROSPACE *Proceedings*

JOURNAL FOR CZECH AEROSPACE RESEARCH

LETECKÝ *zpravodaj*

Editorial address:
Aeronautical Research and Test Institute / VZLÚ, Plc.
Beranových 130, 199 05 Prague 9, Letňany
Czech Republic
Phone.: +420-225 115 223, Fax: +420-869 20 518

Editor-in-Chief: Ladislav Vymětal (e-mail: vymetal@vzlu.cz)
Editor & Litho: Stanislav Dudek (e-mail: dudek@vzlu.cz)

Publisher: Czech Aerospace Manufacturers Association / ALV, Prague
Printing: Studio Winter Ltd. Prague

Published with the assistance of Czech Ministry of Education, Youth and Sports (MŠMT).

Subscription and ordering information available at the editorial address. Legal liability for published manuscripts' originality holds the author. Manuscripts contributed are not returned automatically to authors unless otherwise agreed. Notes and rules for the authors are published at our Internet pages http://www.vzlu.cz/.

Czech AEROSPACE Proceedings
Letecký zpravodaj
1/2007

ISSN 1211 - 877X

Contents / Obsah

L-159B Advanced Jet Training System

Pokročilý výcvikový systém L-159B

Ing. Martin Mamula / Aero Vodochody, Ltd.

Current strategy of placing military jet trainer airplane into integrated system for training is a must for each producer. Aero Vodochody with it's L-159B is no exception.

Vojenský cvičný proudový letoun musí dnes každý výrobce se zvýšeným důrazem pojímat jako součást integrovaného systému pro výcvik. Aero Vodochody se svým letounem L-159B není v tomto ohledu výjimkou.

Keywords: integrated jet training system, military, simulator, light combat aircraft

Past experience

Current trends in military pilot training stress minimum cost of pilot training from the outset to his operational qualification and are subject to careful optimization. This optimization concentrates on the selection of pilot training candidates, preparation of effective training syllabus as well as on the implementation of "train as you fight" principle which realistically prepares trainees for their future operational environment. Today, military flight training is supported by numerous analytical tools, however, many general training principles were implemented intuitively in the past.

For example, former Czechoslovak national aircraft industry which had been a sole supplier of jet pilot training systems for all Warsaw Pact countries (except for Poland) and many Third World Air Forces produced not only aircraft and associated logistics but also various ground based training systems. This can be well illustrated by the L-39 training system developed in late 60s and early 70s which included L-39 Albatros basic and advanced jet trainer, logistic support, KL-39 van mounted test equipment, and various training aids including TL-39 full mission simulator and NKTL-39 ejection trainer. L-39 training system used experience with its predecessor, the training system centred around L-29 Delfin jet trainer and provided training for future pilots of Soviet built planes such as MiG and Sukhoi families of aircraft and F-5, F-16 and Mirage fighters used by some Third World customers. While a majority of L-39s had a cockpit reflecting Soviet fighter technology of the 70s, late production version featured integrated digital avionics with a Head-Up Display needed to provide effective training of F-16 pilots.

After the L-39, another training development milestone occurred in 80s while Czechoslovak aviation industry was engaged in a development of new Warsaw Pact jet trainer intended for training pilots of then new fighter aircraft such as MiG-29, Su-24M, Su-27 or MiG-31. Resulting L-39MS aircraft featured improved flight performance and integrated avionics with HUD, tactical info presentation, inertial navigation system and many similarities to advanced Soviet fighters. Development was finished just before political changes in 1989 and the L-39MS was delivered just to the Czechoslovak Air Force. Its export form, the L-59 trainer was delivered to Egypt and Tunisia and the L-39MS/59 programme provided valuable experience with new training technologies.

Aero L-39 Albatros (left) was the first turbofan powered jet trainer in the world and it was supported by what is today called "Total Training System" (+TL-39, NKTL-39 etc. - above)

Aero Approach to Military Jet Training

Current activities of Aero Vodochody in the field of military pilot training are based on its past experience, current military-political situation, results of L-159 Advanced Light Combat Aircraft programme and use of latest technologies.

Military-political environment

Aero understands that current conditions for jet pilot training are driven by general military-political factors which have following characteristics:

- Military budgets are limited after military-political changes in 1990's
- Numbers of military equipment are steadily decreasing, however, its complexity is increasing. This highlights the need for effective training
- Importance of military equipment affordability increases
- Revolution in military affairs (RMA) increases importance of information on the battlefield
- Types of military and non-military threats widen their range, require various mission scenarios and drive the use of military aviation into asymmetric warfare conditions
- Military aircraft are being purchased in relatively low numbers and required numbers of pilots trained are decreased. This situation calls for joint training solutions involving several air forces
- Relative percentage of multi-role combat aircraft increases and number of mission types performed by single aircraft type increases

L-159 Advanced Light Combat Aircraft

The L-159 Advanced Light Combat Aircraft was developed in nineties in order to fulfil Czech Air Force requirement for light multi-role combat aircraft. While, the two-seat training version was not required by the customer, the single-seat L-159 was developed with a two-seat training version in the mind. The L-159 airframe is modular and can be used for both single and two-seat versions with minimum changes. For Aero Vodochody, the L-159 was important milestone since it introduced advanced western components and systems including Honeywell F124 military turbofan engine and digital integrated avionics.

The L-159 represents advanced light multi-role combat aircraft which fully utilizes advanced western technologies and due to its good flight performance provides an excellent basis for training aircraft. (Photo Jan Kouba)

The L-159B Advanced Training System

After accumulating experience with the L-159 and having access to latest western technology, in 1999 Aero decided to develop the L-159B Advanced Training System (ATS). The primary objective of the L-159B ATS is to offer a comprehensive training system for the advanced and operational training of military pilots. The system includes the aircraft, logistic and training systems as well as equipment for mission planning and debriefing which is seen as highly important due to increasing influence of mission planning and debriefing phases on effectiveness of combat missions.

The key part of the system is the L-159B Advanced Jet Training aircraft. The L-159B was specifically designed to fulfil current training needs on training of pilots of latest generation of multirole combat aircraft. The L-159B Albatros II is a subsonic platform, since Aero philosophy reflects the opinion that supersonic training aircraft typically have unnecessarily high acquisition and operational costs. Due to carefree handling characteristics of new fighter generation, supersonic aircraft performance and handling is not seen as critical and the L-159B design concentrates on the operation of typical fighter systems in representative mission environment at subsonic speeds.

Advanced Multi-Role Combat aircraft are extremely expensive and are being purchased in limited numbers. This stresses a need for adequate training since peacetime mishaps and combat losses have a great impact on the operational capability of the Air Force. E.g. Czech Air Force have got just fourteen JAS-39 Gripen fighters compared to hundreds of MiG-21s used in the past.

Typical fighter aircraft systems had to be installed onboard the L-159B to make sure that the pilots are trained in the same environment and operate the systems and weapons as used in a combat aircraft. This also gives the L-159B significant weapon training and combat capability. With the weapon control systems, electronic countermeasures and/or target acquisition sensors, the L-159B can be deployed to carry out air-to-air, air-to-ground and tactical air reconnaissance missions. This also makes the L-159B an effective and affordable system for homeland security and combat missions against dispersed threats where the use of supersonic fighters is not effective.

L–159B — Basic Technical Data

Length:	**12.72 m**
Wingspan:	**9.54 m**
Height:	**4.87 m**
Empty weight:	**4,350 kg**
Maximum takeoff weight:	**8,000 kg**
Maximum speed:	**936 km/h**
Service ceiling:	**13,200 m**

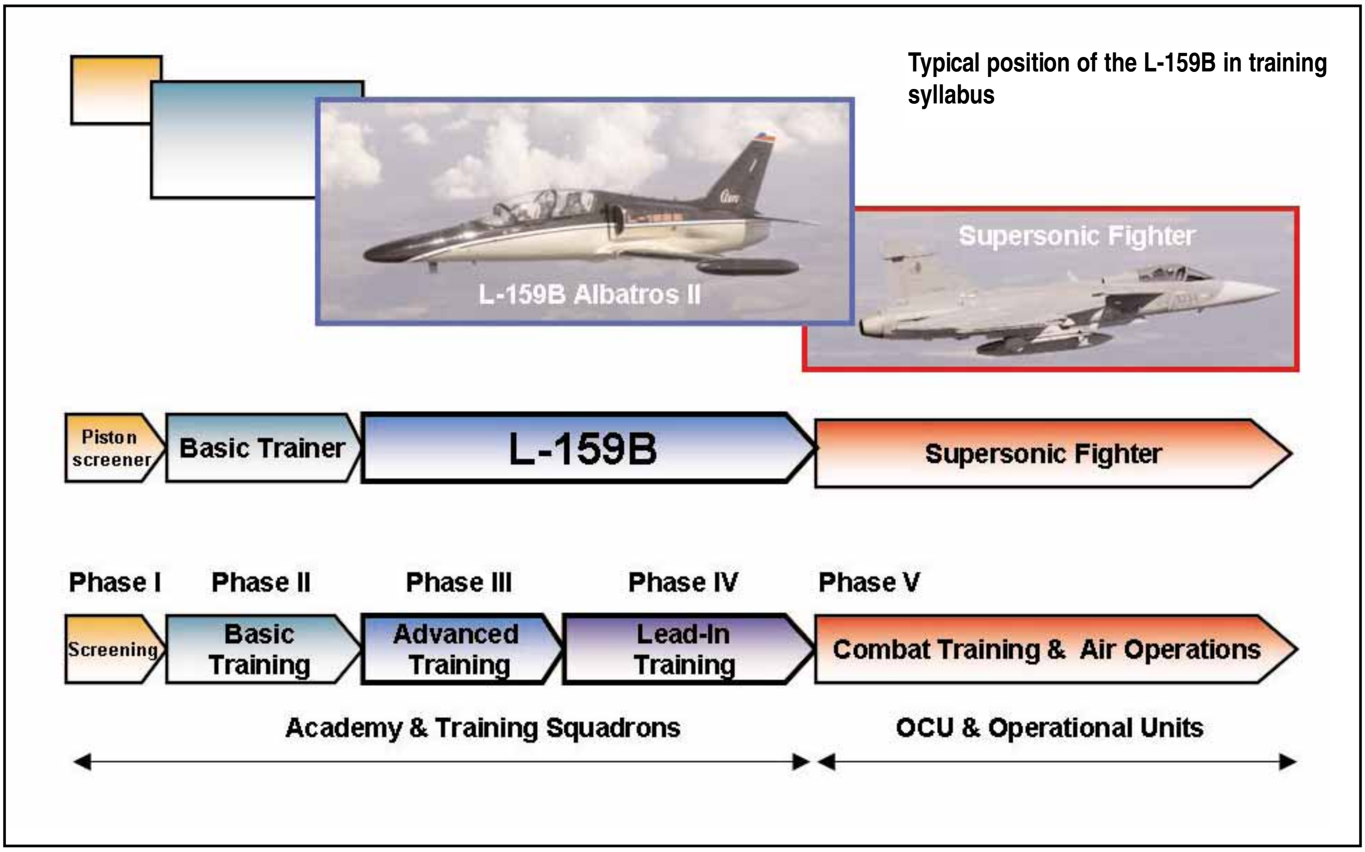
Typical position of the L-159B in training syllabus

Design features

The L-159B design concentrates on several areas which are seen as critical for training effectiveness. Firstly, the crew station was designed in order to be fully compatible with the design of the new generation multi-role supersonic combat aircraft cockpits. This approach is essential for an efficient training free from ”negative training“ which is not unusual in other training systems using older ”analogue“ platforms. Also, open systems architecture avionics includes typical fighter systems and has sufficient growth capability to include sophisticated simulations of onboard systems such as multimode radar or electronic warfare suite. In addition, powerful F124 turbofan engine provides the aircraft with the flight dynamics required to perform typical combat manoeuvres. To support training of the whole mission cycle, aircraft systems support integrated mission planning and data transfer and onboard digital recording of flight and system parameters and video.

In order to download costly training missions from combat aircraft, the L-159B is also designed for compatibility with Night Vision Goggles and has a provision for in-flight refuelling system. All aircraft systems comply with western standards and their selection and design supports training in NATO operational procedures.

Logistic Support

Customers are becoming increasingly aware of importance of life cycle cost and parameters such as reliability, availability, mean time between repairs, mean time of technical repair etc. These parameters can be largely influenced by careful design of the aircraft and optimized logistic system.

L-159B ATS includes integrated logistics support package which consists of logistic support analysis and resulting recommendations to customer, delivery of logistic documentation, design and production of Ground Support Equipment and tools and of course supply of spare parts.

Ground Based Training

In the past Aero aircraft were typically delivered with ground based training devices including Full Mission Simulators from Czech Letov company. After changes in Czech aeronautical industry during nineties, new potential suppliers evolved. For the L-159B, Aero teamed with E-COM Slavkov, a well established supplier of simulation technology. Both companies, supported by Czech Ministry of Industry and Trade developed new full mission simulator (FMS) for the L-159B. The L-159B FMS utilizes advanced commercial technology which makes it much more affordable than older generation systems based on specific military components.

While the FMS can be considered as a pinnacle of L-159B Ground Based Training, the system also includes other devices such as Part Task Trainers used to familiarize pilots to particular tasks or multimedia documentation.

L-159B Full Mission Simulator uses latest commercial components in order to provide affordable operation and long-term supportability

Mission Planning and Debriefing

Today, military pilots fly missions which no longer consist of just flying the aircraft. They are required to fly optimum approach to target minimizing aircraft exposure to enemy threats, use their weapons in optimum manner and fully utilize on-board sensors in order to maximize their performance. This is the reason while mission planning and debriefing systems form an integral part of fighter aircraft support systems.

Thus it is important to train pilots for detailed mission preparation and debriefing. L-159B ATS includes mission planning module based on the PC type of computer and when the mission data file including waypoints, flight plans, communication and identification systems presets and weapon delivery profiles, pilot load it onto Data Transfer Cartridge which is loaded into receptacle in the aircraft and all the data is loaded into onboard computer.

After the flight, digital video, flight data, pilot activities and systems status can be retrieved from the same cartridge and the mission can be rehearsed on special on-board console which enables time synchronize debriefing from multiple aircraft.

Conclusions

”Total Training Systems“ represent affordable and effective solution training of military pilots. Evaluation and Testing of the L-159B ATS which concentrated on all its elements shows it extensive potential. This is being confirmed by evaluations by potential customers who use aircraft so diverse as F-16, MiG-29 or Mirage 2000.

Mission Debriefing station uses various video and data presentations including 3D flight presentation

Comparative Study of Conventional and Tandem - Wing Aircraft Configuration

Srovnávací studie konvenčního a tandemového uspořádání nosných ploch letounu

Zdeněk Pátek, Jan Červinka / VZLÚ, Plc., Prague

Fundamental aerodynamic characteristics (maximum lift and drag in cruise flight) of two light general aviation configurations are compared. The configurations are a conventional and a tandem-wing airplane. Both of the configurations have equal total area of the wing - horizontal tail unit and tandem - wing respectively, equal fuselages and equal wetted surfaces. The maximum lift and drag in the cruise flight are evaluated for a large range of positive and negative static margins using AAA method.

Pro dvě konfigurace malého letounu všeobecného letectví, pro konvenční konfiguraci a pro letoun s tandemovým křídlem, byly srovnávány základní aerodynamické charakteristiky (maximální vztlak a odpor v cestovním letu). Obě konfigurace se vyznačují shodným trupem, stejnou celkovou plošnou velikostí křídla s vodorovnou ocasní plochou resp. tandemového křídla a stejnou omočenou plochou. Maximální vztlak a odpor v cestovním letu jsou vypočteny metodou AAA pro široký rozsah kladných i záporných statických zásob.

Keywords: wing, configuration, conventional, tandem, lift, drag, comparison.

1. Introduction

The conventional configuration of aeroplane, i.e. a wing followed by a horizontal tail unit equipped with an elevator is by far the most widespread configuration in today general aviation. Most of the aircraft´ s lift is generated by the wing, the lift of the tail unit is small and could be negative. The conventional configuration of aircraft has been developed for a century, so it seems to take a matured concept where the future aerodynamic development will bring rather modest improvements. Consequently, different unconventional concepts draw attention. One of the unconventional configurations is represented by a tandem-wing concept [1], [2], [3].

2. Tandem-wing configuration

The main distinctive part of this configuration is represented by the tandem-wing, in fact two wings of the approximately equal dimensions, especially equal span and equal area. One of the surfaces is equipped with an elevator. The aerodynamic benefit should be in the better lift-to-drag ratio and higher maximum lift. The beneficiary phenomena should be created by the fact that the lift both of the fore and aft wings is positive. So contrary to the conventional configuration, the induced drag should be caused exclusively by the positive oriented lift of surfaces of relatively high aspect ratios and as a consequence, the induced drag should be lower for the equal total lift. Also mutual positive aerodynamic influence of coupled wings is presented as a beneficial factor.

3. Compared configurations

Two configurations of a light small general aviation aircraft were studied - a conventional A configuration and tandem-wing B configuration (see Figs. 1 and 2). For the purpose of the fair comparison:

- the total area of the wing and tail unit areas of A configuration was equal with the total area of the wings (fore and aft) of B configuration
- the aspect ratios of the wing of A and the aft wing of B were identical
- the taper ratios of the wing of A and the aft wing of B were identical
- the tail unit of A configuration was designed with an symmetrical airfoil section often used for the horizontal tail units
- the fore-wing of the B configuration was designed with specific laminar airfoil section often used for the canards and fore-wings
- the fuselages were identical

So it is reasonable to suppose the wetted areas and then the values of skin friction drags were equal and do not distort the overall results. The fundamental geometric data are presented in Tables 1 and 2.

Nomenclature

C_D	drag coefficient
C_L	lift coefficient
C_{LMAX}	maximum lift coefficient
S	lifting surfaces area
SM	static margin
AR	aspect ratio
TR	taper ratio
δ_c	fore-wing elevator deflection
δ_h	horizontal tail elevator deflection

Fig. 1

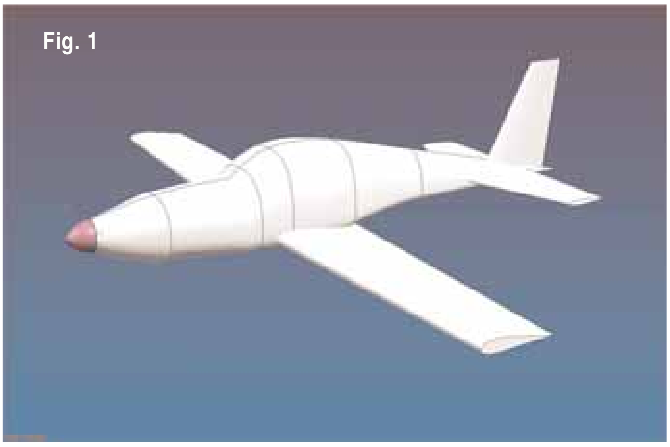

Table 1 — A Configuration

Wing area	8.00
Wing aspect ratio	10.6
Wing taper ratio	0.667
Horizontal tail unit area	2.00
Horizontal tail unit aspect ratio	4.50
Horizontal tail unit taper ratio	0.50
Total area	10.00

Table 2 — B Configuration

Fore-wing area	5.48
Fore-wing aspect ratio	8.75
Fore-wing taper ratio	0.45
Aft-wing area	4.52
Aft-wing aspect ratio	10.6
Aft-wing taper ratio	0.667
Total area	10.00

The conventional configuration has conventional tail unit equipped with the elevator, the elevator chord aft of the hinge line is 25% of the tail unit chord, the maximum deflection up is 30 degrees.

The tandem-wing configuration is equipped with the elevator on the foreplane (fore-wing), the control surface chord aft of the hinge line is 25% of the foreplane chord, the maximum elevator deflection down is 22 degrees.

4. Computational method

Both of the configurations were evaluated in the same manner. The Advanced Aircraft Analysis software (by DAR Corporation) was used, see [4], [5].

Two main criteria were assessed:

1) Maximum lift ($C_{LMAX} \cdot S$)
2) Drag ratio at cruise conditions

The assessment was elaborated for the large range of static margin of the two aircraft. The positive as well as negative (i.e. statically unstable case) were treated to obtain an overall view on the problem. Equal weights of the both configurations were supposed.

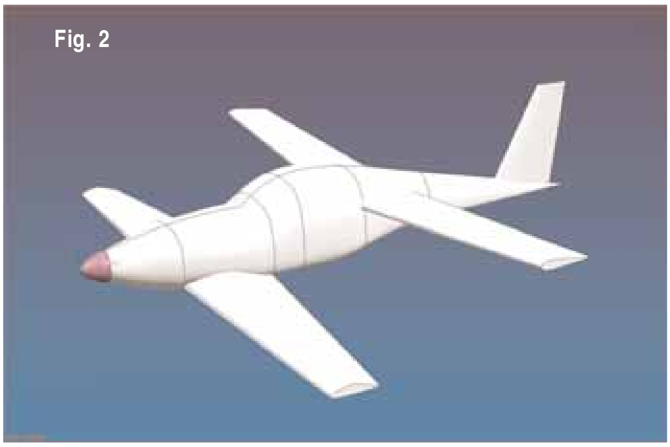

Fig. 2

Table 3 — A Configuration

SM	-5	0	5	10	15	20	25	30
$C_{L MAX}$	1.657	1.625	1.594	1.564	1.535	1.508	1.391	1.172
$C_{L MAX} \cdot S$	13.256	13.000	12.752	12.512	12.280	12.064	11.128	9.376
δ_h [deg]	7.67	2.97	-1.54	-5.88	-10.07	-16.17	-30.00	-30.00
Limit	$C_{L MAX}$ wing	$C_{L MAX}$ wing	$C_{L MAX}$ wing	$C_{L MAX}$ wing	$C_{L MAX}$ wing	$C_{L MAX}$ wing	elevator deflection	elevator deflection

Table 4 — B Configuration

SM	-5	0	5	10	15	20	25	30
$C_{L MAX}$	1.490	1.625	1.648	1.625	1.438	1.219	1.057	0.930
$C_{L MAX} \cdot S$	14.900	16.250	16.480	16.250	14.380	12.190	10.570	9.300
δ_c [deg]	-3.4	2.7	8.5	14.7	22.0	22.0	22.0	22.0
Limit	$C_{L MAX}$ aft-wing	$C_{L MAX}$ aft-wing	$C_{L MAX}$ aft-wing	$C_{L MAX}$ fore-wing	elevator deflection	elevator deflection	elevator deflection	elevator deflection

Table 5 — A Configuration

SM	-5	0	5	10	15	20	25	30
C_D	0.0424	0.0419	0.0415	0.0411	0.0409	0.0416	0.0421	0.0429
$C_D \cdot S$	0.3393	0.3351	0.3318	0.3290	0.3271	0.3325	0.3369	0.3429

Table 6 — B Configuration

SM	-5	0	5	10	15	20	25	30
C_D	0.0316	0.0309	0.0303	0.0297	0.0292	0.0287	0.0283	0.0282
$C_D \cdot S$	0.3162	0.3090	0.3025	0.2967	0.2916	0.2871	0.2834	0.2822

5. Results

Results are presented in Tables 3 to 5 and in Figures 3 to 6. The limit in the tables means decisive phenomenon that limited the value of C_{LMAX}.

The values of static margin are pronounced in terms of the mean aerodynamic chords of the main wings of respective configurations, i.e. the wing of the conventional A configuration and the fore-wing of the tandem-wing B configuration respectively.

It is evident that the conventional configuration can achieve higher maximum lift than the tandem-wing at higher positive static margins. With the centre of gravity approaching the aerodynamic focus, the tandem-wing

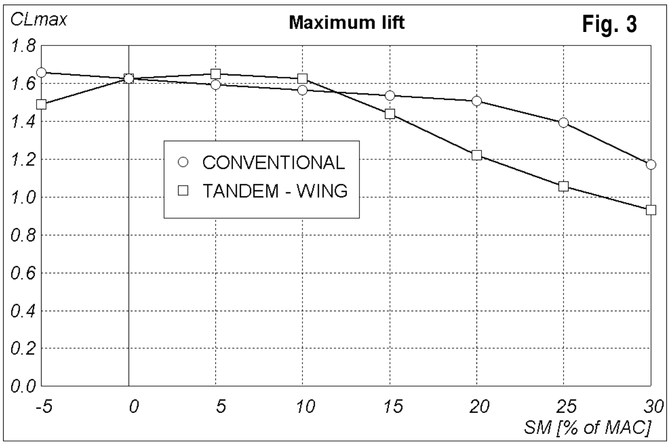

Fig. 3

continuously gains and for negative static margins the supremacy is substantial.

On the other hand, the conventional configuration is evidently less sensitive to the static margin changes. The tandem-wing configuration is relatively highly sensitive to the static margin. The static margin sensitivity should be a source of concern during design phases, as very different causes of maximum lift limit could be reached: stall of the fore-wing, stall of the aft-wing and maximum deflection of the elevator on the fore-wing. The stall of the airplane caused by the stall of the aft-wing is typical of the negative and small positive static margins. This case could be extremely dangerous in flight as it is accompanied by a strong nose-up pitching moment, it would be impossible to use such static margins with conventional control systems without active control. So the small static margin advantage is less usable and less useful than seems to be at first sight, at least for general aviation aircraft.

As far as the drag at cruising conditions is concerned (tables 5 and 6), the tandem-wing configuration features lower overall drag than the conventional configuration for all static margins under the same conditions.

6. Conclusions

The conventional and tandem-wing configurations of a general aviation aeroplane were compared. The both configurations have the equal total area of the lifting surfaces. The results show that tandem-wing can achieve higher maximum lift under certain conditions and it can achieve lower overall drag in cruise flight. But the tandem-wing is also very sensitive to static margin changes and also a potentially very dangerous case of the stall of the aft-wing could occur for the negative and low positive static margins. The use of this configuration for a general aviation airplane should be very rigorously examined during design phases.

References:

[1] Laitone, E.V.: *Prandtl's Biplane Theory Applied to Canard and Tandem Aircraft*; Journal of Aircraft, Vol. 17, No. 4, April 1980, pp. 233-237

[2] Kroo, I.: *A General Approach to Multiple Lifting Surface Design and Analysis*; AIAA Paper AIAA-84-2507

[3] Wolkovitch, J.: *Subsonic VSTOL Aircraft Configurations with Tandem Wings*; Journal of Aircraft article No.78-1504R

[4] Roskam, J.: *Airplane Design*; Roskam Aviation and Engineering Corporation, Ottawa, Kansas, 1987

[5] *Advanced Aircraft Analysis version 3.0*, DAR Corporation, Lawrence, Kansas, 2005

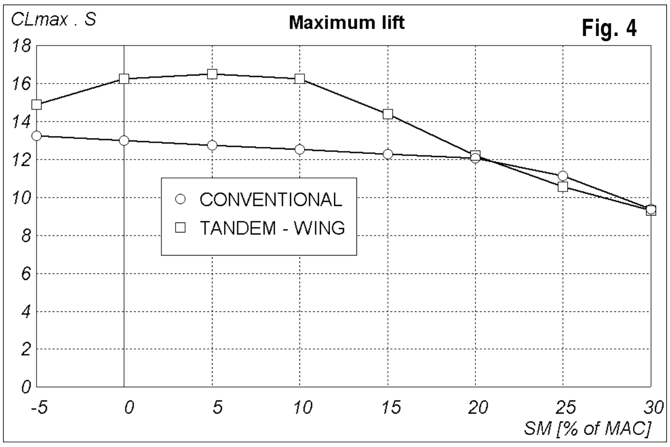

Fig. 4

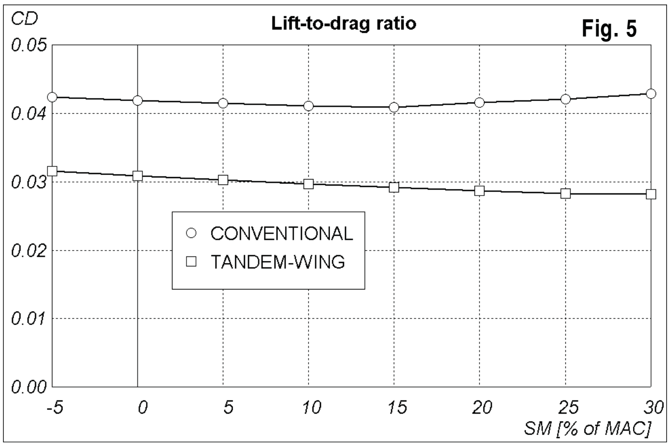

Fig. 5

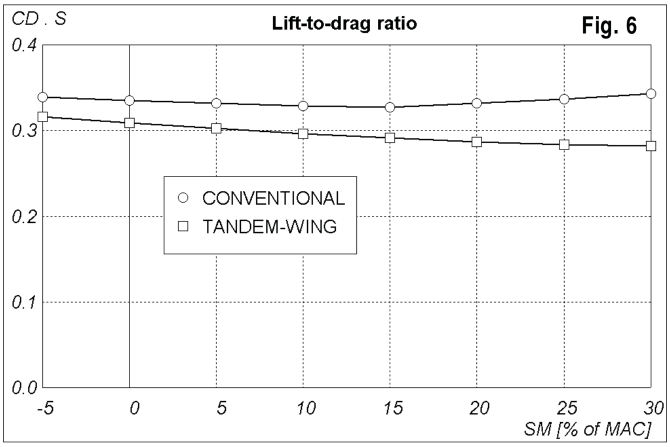

Fig. 6

Acknowledgments

The research was supported by the MSM0001066901 *Applied External Aerodynamics Development* (Rozvoj aplikované vnější aerodynamiky) project supported by the Ministry of Education, Youth and Sports of the Czech Republic.

Calculations of Wing Loading Distribution Using the Matrix Formulation

Výpočet zatížení křídla užitím maticového počtu

Prof. Ing. Antonín Píštěk, CSc / Institute of Aerospace Engineering, Brno University of Technology, Brno

An aeroplane is influenced by a wide spectrum of loads during operations. The spectrum of loads is given by flight and landing load cases, mass and operation configurations leading to a great number of load cases that all have to be taken into consideration for loading of an aeroplane. The automation of computation is necessary and cannot be done without modification of the computation methodology. The paper describes the process of wing loading computation using a matrix formulation. This formulation simplifies the solution of complicated and time consuming dynamic loading, caused by numerical methods, and enables the selection of the essential loads in a uniform data basis. Explanation is based on an example of a wing loading. The method described in this paper was successfully applied in the CAE system to aeroplane loading computation, named SAVLE (System for Automation of Load Calculation of Aeroplanes), which was used in the Czech aircraft industry during the development of several aeroplanes.

Letoun je podroben širokému spektru zatížení během provozu, které je dáno letovými a přistávacími případy zatížení, hmotovými konfiguracemi dalšími podmínkami. Tyto kombinace vedou k velkému počtu případů zatížení, které musí být zahrnuty do hodnocení zatížení letounu. Automatizace výpočtů je nezbytná a vzhledem k časové náročnosti je žádoucí i modifikace metodiky výpočtu. V článku je popsán postup výpočtu zatížení konstrukce typu křídlo užitím maticového počtu. Tento přístup zjednodušuje řešení složitých, časově náročných výpočtů, umožňujících rychlý výběr rozhodujících zatížení. Metoda byla úspěšně použita v systému SAVLE (Systém Automatizovaného Výpočtu zatížení LEetadel), který je stále používán prakticky ve všech podnicích českého leteckého průmyslu.

Keywords: aircraft, load distribution, matrix, automation.

General Introduction

The wing is most frequently loaded by three types of aerodynamic loading, namely, by the effects of lift forces, drag forces and moments. Loading in the direction of the lift force is given by the distribution of lift over the wing span for the basic loading up to the influence of deflected flaps, ailerons, fuselage influence etc. The loading in the direction of drag is defined by the drag coefficients of particular structural parts. Similarly, the torque moment loading is defined by appropriate moment coefficients. The principle of the described method is division of the wing into an arbitrary number of wing segments for which the angles of dihedral and sweepback are constant and the unit loading is computed independently for each wing segment along the wing span.

Fig. 1 shows the division into segments and the resulting loading components in wing cross-sections along the wing span. It is possible to compute 6 components of resulting loading for the defined wing cross-section ***r***

$$\mathbf{Z}_r = \{\ \mathbf{T_N\ T_T\ N\ M_N\ M_T\ M_K}\ \}$$

Load of aircraft structural parts

Aircraft loads estimation is generally divided into:

- calculation of wing load, tail units, fuselage etc. by air forces
- load calculation by weight and inertial forces,
- load calculation by landing load cases.

The load calculation method is a part of the SALVE system, where each case of load is uniquely determined by a data sequences .The most important data are — weight, speed, control surfaces deflections, load factors, rotation accelerations, aerodynamic characteristics (angle of attack, lift, drag and moments coefficients, mass characteristics, power unit loads, landing gear forces etc.) The data set is called ”*load case data record*“ and it includes about 180 data items. This article deals with wing load calculation method from aerodynamic forces.

Wing Design Loads

Design wing loads consist of the shearing forces, bending moments and torsions as a result of air pressures along the wing span. The main loads limits are given by V-n diagrams for maneuver, for gust envelope and other flight conditions which are associated with control surface deflection, landing condition etc. Aerodynamic load spanwise distribution consists of two parts: basic loading (normal) and additional loading (effects of fuselage, nacelle, flaps, deflected ailerons, damping etc.

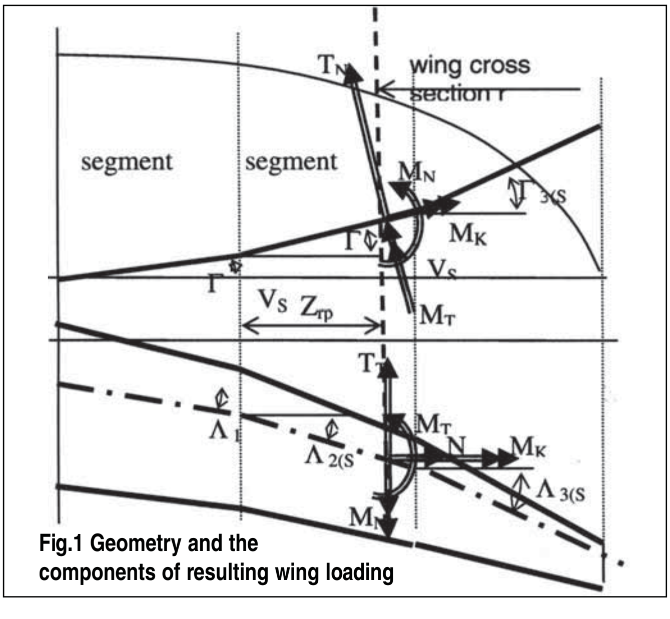

Fig.1 Geometry and the components of resulting wing loading

Wing load by aerodynamic forces is represented by loads

- — in lift direction,
- — in drag direction,
- — by moment effect.

Each of mentioned types has different manner of definition and also different way of calculation of wing load components.

Load in lift direction is given by local lift coefficient diagram $\mathbf{c_L}^{\mathbf{i}}$ and local chord length of wing $\mathbf{c_r}$. Each type of load distribution depends on the angle of attack and characteristic value for example $\mathbf{c_{LW}}$ for the normal load distribution etc. We get in the given cross-section **r** for each load distribution the value called the first integral — shearing forces and the second integral — bending moment, for unit aerodynamic coefficients. Load in lift direction is set by spreading of local coefficient of pressure along the $\mathbf{C_L}^{\mathbf{i}}$ and local depth of wing $\mathbf{C_r}$. Each type of spreading is dependent on the angle of attack and characteristic quantity for example $\mathbf{C_{LW}}$ for the normal distribution etc. We get a value in the given cross-section for each distribution. This is called the first integral — moving force and the second integral — bending moment, for unit aerodynamic coefficients, for example $\mathbf{C_{LW}} = \mathbf{1}$.

Load in drag direction is defined with drag coefficient related to wing area and with geometry structural parts along wing span. The load acting in drag direction and the value is usually proportional to wing chord. The load is the product of local drag coefficient and local wing chord ($\mathbf{c_{Dr}}\ \mathbf{c_r}$). The first and the second integral calculation will be done again for individual drag coefficients and parts.

Load with moment effect — is set by value of local moment coefficient $\mathbf{c_m}$ and local wing chord $\mathbf{c_r}$, where the unit load is calculated for product ($\mathbf{c_{mr}}\ .\ \mathbf{c_r}^{\mathbf{2}}$). The first integral value means the torsion moment.

The Basic Transformation

The basic transformational relationship distributes the loads in lift direction, drag direction and moment into the local coordinate system of wing cross-section using the following relations.

$$c_n = c_L\ .\ \cos\ \alpha + c_D\ .\ \sin\ \alpha$$
$$c_t = c_L\ .\ \sin\ \alpha + c_D\ .\ \cos\ \alpha$$
$$c_m = c_m$$

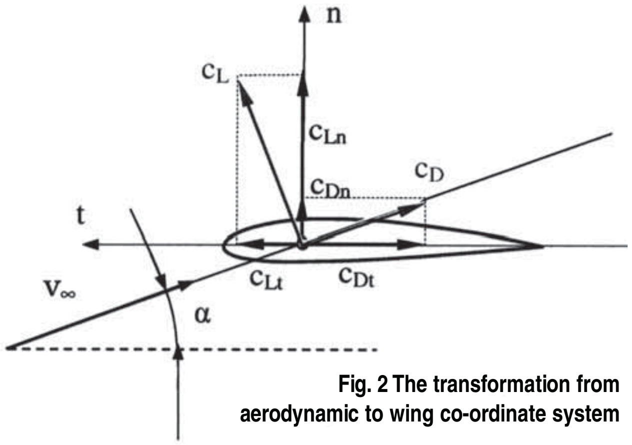

Fig. 2 The transformation from aerodynamic to wing co-ordinate system

We arrange the matrix of aerodynamic coefficients transformed to wing coordinate system.

$$\mathbf{C} = \begin{bmatrix} c_n^1 & c_n^2 \ldots & c_n^{ild} \ldots & c_n^{nld} \\ c_t^1 & c_t^2 \ldots & c_t^{ild} \ldots & c_t^{nld} \\ c_m^1 & c_m^2 \ldots & c_m^{ild} \ldots & c_m^{nld} \end{bmatrix}$$

This matrix is arranged just once for all solved load cases. The next matrixes are vectors of unit first and second integrals for each individual air loading distribution in cross-section ***r***.

$$\mathbf{T_r^s} = \left\{ T_r^1 \quad T_r^2 \ldots \quad T_r^{ild} \ldots \quad T_r^{nld} \right\}$$

$$\mathbf{M_r^s} \quad \left\{ T_r^1 \quad T_r^2 \ldots \quad T_r^{ild} \ldots \quad T_r^{nld} \right\}$$

These matrixes are arranged for solved cross-section r on wing segment **s** by all type loads distribution computed in wing projection plane. Integration is carried out separately in individual wing segment **s**.

Transformational relationship for loads in the normal direction, $\mathbf{c_{Ln}}$ and $\mathbf{c_{Dn}}$

$$T_N^r = T_R^r / \cos \Gamma_s$$

$$T_T^r = 0$$

$$M_N^r = M_R^r . z_{RP} / \cos^2 \breve{A}_s$$

$$M_T^r = 0$$

$$M_K^r = T_R^r . z_{RP} / \cos^2 \breve{A}_s . \sin \ddot{E}_s$$

$$N^r = 0$$

Transformational relationship for loads in tangent direction, $\mathbf{c_{Lt}}$ and $\mathbf{c_{Dt}}$

$$T_N^r = 0$$

$$T_T^r = T_R^r$$

$$M_N^r = 0$$

$$M_T^r = -z_{RP} / \cos \breve{A}_s$$

$$M_K^r = 0$$

$$N_r = 0$$

Transformational relationship for loads from $\mathbf{c_m}$

$$T_N^r = 0$$

$$T_T^r = 0$$

$$M_N^r = 0$$

$$M_T^r = 0$$

$$M_K^r = T_R^s / \cos \breve{A}_s$$

The given relationships we include into transformational matrixes

$$\mathbf{T}_{\mathbf{G}}^{\mathrm{s}} = \begin{bmatrix} 1/\cos\text{Ă}_s & 0 & 0 \\ 0 & 1 & 0 \\ -1/\cos^2\text{Ă}_s & 0 & 0 \\ 0 & -1/\cos\text{Ă}_s & 0 \\ \sin\text{Ë}_s/\cos^2\text{Ă}_s & 0 & 1/\cos\text{Ă}_s \\ 0 & 0 & 0 \end{bmatrix}$$

$$\mathbf{M}_{\mathbf{G}}^{\mathrm{s}} = \begin{bmatrix} 0 & 0 & 0 \\ 0 & 0 & 0 \\ 1/\cos^2\text{Ă}_s & 0 & 0 \\ 0 & 1/\cos\text{Ă}_s & 0 \\ -\sin\text{Ë}_s/\cos^2\text{Ă}_s & 0 & 0 \\ 0 & 0 & 0 \end{bmatrix}$$

The upper matrixes $\mathbf{T}_{\mathbf{G}}^{\mathrm{s}}$ and $\mathbf{M}_{\mathbf{G}}^{\mathrm{s}}$ are valid for all cross-sections of wing segment **s**.

The next matrix defines the position of cross-section **r** measured from left margin of wing segment **s**

$$\mathbf{T}_{\mathbf{G}}^{\mathrm{r}} = \begin{bmatrix} 1 & 1 & 1 \\ 1 & 1 & 1 \\ z_{rp} & 1 & 1 \\ 1 & z_{rp} & 1 \\ z_{rp} & 1 & 1 \end{bmatrix}$$

This simple matrix is assembled for solved cross-section **r** given by co-ordinate **zrp**.

Using the matrix operation

$$\mathbf{Z}_{\mathbf{rs}} = (\mathbf{T}_{\mathbf{G}}^{\mathrm{r}} * \mathbf{T}_{\mathbf{G}}^{\mathrm{s}} .\ \mathbf{C} .\ \mathbf{T}_{\mathbf{r}}^{\mathrm{s}} + \mathbf{M}_{\mathbf{G}}^{\mathrm{s}} .\ \mathbf{M}_{\mathbf{r}}^{\mathrm{s}} .\ \mathbf{C})\ \mathbf{q}$$

we receive all loads components in cross-section **r** which is

$$\mathbf{Z}_r = \{\ \mathbf{T_N}\ \mathbf{T_T}\ \mathbf{N}\ \mathbf{M_N}\ \mathbf{M_T}\ \mathbf{M_K}\ \}$$

where,

$\mathbf{T}_{\mathbf{G}}^{\mathrm{r}}$ matrix of wing cross section **r** position

$\mathbf{T}_{\mathbf{G}}^{\mathrm{s}}$ transformation matrix of forces for wing segment geometry *s* in cross section ***r***

$\mathbf{T}_{\mathbf{r}}^{\mathrm{s}}$ matrix of the unit forces (the first integral) on section *s* for wing cross section ***r*** for all types of aerodynamic load distributions,

$\mathbf{M}_{\mathbf{G}}^{\mathrm{s}}$ transformation matrix of moments for wing section geometry *s* in cross section ***r***

$\mathbf{M}_{\mathbf{r}}^{\mathrm{s}}$ matrix of the unit moments (the second integral) on section *s* for wing cross section ***r*** for all types of aerodynamic load distributions,

C matrix of aerodynamic coefficients for individual types of aerodynamic distributions transformed into structural co-ordinate system,

$\mathbf{T}_{\mathbf{v}}^{\mathrm{s}}$ transformation matrix incorporating the influence of section s geometry and foregoing section ***s+1***

$\mathbf{Z}_{V(s+1)}$ matrix of the resulting loading at the point of modified section s geometry

q dynamic pressure

r index of wing cross section

s index of wing segment

Remind that operator * represents a scalar multiplication of each element of both matrixes. Each wing segment ***s*** is defined at position, where the wing dihedral angle and (or) wing sweep angle changes. For influence of wing segment ***s*** to ***s-1*** we use the loads components in point $\mathbf{V}_s$. The transformation relations depend on change of wing sweep angle.

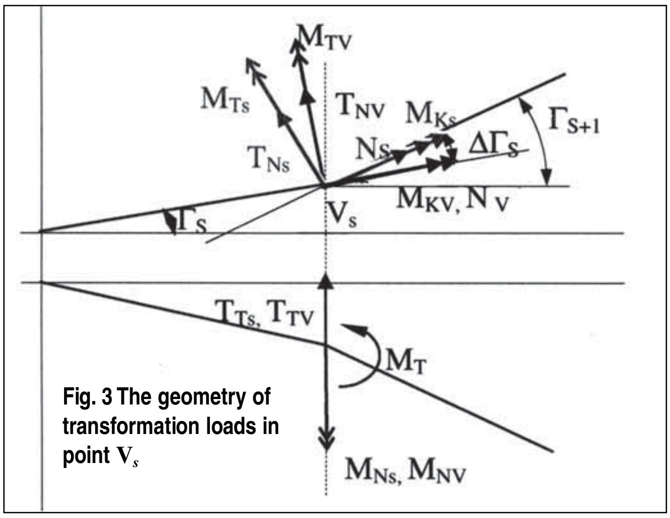

Fig. 3 The geometry of transformation loads in point $\mathbf{V}_s$

$$\mathbf{T_{NV}} = \mathbf{T}_{\mathbf{N}s} .\ \mathbf{cos}\ \Delta\Gamma_s + \mathbf{Ns} .\ \mathbf{sin}\ \Delta\Gamma_s$$
$$\mathbf{T_{TV}} = \mathbf{T}_{\mathbf{T}s}$$
$$\mathbf{M_{NV}} = \mathbf{M}_{\mathbf{N}s}$$
$$\mathbf{M_{TV}} = \mathbf{M}_{\mathbf{T}s} .\ \mathbf{cos}\ \Delta\Gamma_s + \mathbf{M}_{\mathbf{K}s} .\ \mathbf{sin}\ \Delta\Gamma_s$$
$$\mathbf{M_{KV}} = \mathbf{M}_{\mathbf{K}s} .\ \mathbf{cos}\ \Delta\Gamma_s - \mathbf{M}_{\mathbf{T}s} .\ \mathbf{sin}\ \Delta\Gamma_s$$
$$\mathbf{N_V} = -\mathbf{T}_{\mathbf{N}s} .\ \mathbf{sin}\ \Delta\Gamma_s + \mathbf{N}_s .\ \mathbf{cos}\ \Delta\Gamma_s$$

The upper relations are in matrix form as follows:

$$\mathbf{T}_{\mathbf{v}}^{\mathrm{s}} = \begin{bmatrix} \cos\Delta\Gamma_s & 0 & 0 & 0 & 0 & \sin\Delta\Gamma_s \\ 0 & 1 & 0 & 0 & 0 & 0 \\ 0 & 0 & 1 & 0 & 0 & 0 \\ 0 & 0 & 0 & \cos\Delta\Gamma_s & \sin\Delta\Gamma_s & 0 \\ 0 & 0 & 0 & -\sin\Delta\Gamma_s & \cos\Delta\Gamma_s & 0 \\ -\sin\Delta\Gamma_s & 0 & 0 & 0 & 0 & \cos\Delta\Gamma_s \end{bmatrix}$$

This matrix is arranged for each origin of wing segment. The loads in origin of segment s are calculated by matrix operation

$$\mathbf{Z}_{\mathbf{v}s} = \mathbf{T}_{\mathbf{v}}^{\mathrm{s}} .\ \mathbf{Z}_{rs+1}$$

Where $\mathbf{Z}_{rs+1}$ are loads in origin of wing segment **s+1** for $\mathbf{z}_{rp} = \mathbf{0}$

The resultant loads is given by sum of loads in cross-section **r** and loads acting in origin of previous wing segment **s+1**, using the following transformation:

$$\mathbf{T_{Ns}} = \mathbf{T_{NVS}}$$
$$\mathbf{T_{TS}} = \mathbf{T_{TVS}}$$
$$\mathbf{M_{NS}} = \mathbf{M_{NVS}} + \mathbf{T_{NVS}} .\ \Delta z_{rs}$$
$$\mathbf{M_{Ts}} = \mathbf{M_{Tvs}} + \mathbf{N}_{vs} .\ \Delta\mathbf{z_{rs}}$$
$$\mathbf{M_{Ks}} = \mathbf{M_{Kvs}} - \mathbf{T}_{\mathbf{NV}s} .\ \Delta\mathbf{z}_{rs} .\ \mathbf{sin}\ \Lambda\mathbf{s}$$
$$\mathbf{N_S} = \mathbf{N_{VS}}$$

The upper relationships can be written to the matrix form

$$\mathbf{T}_{\mathbf{v}r}^{\mathrm{s}} = \begin{bmatrix} 1 & 0 & 0 & 0 & 0 & 0 \\ 0 & 1 & 0 & 0 & 0 & 0 \\ \Delta z_{rs} & 0 & 1 & 0 & 0 & 0 \\ 0 & \Delta z_{rs} & 0 & 1 & 0 & \Delta z_{rs}.\sin\Lambda_s \\ -\Delta z_{rs}.\sin\Lambda_s & 0 & 0 & 0 & 1 & 0 \\ 0 & 0 & 0 & 0 & 0 & 1 \end{bmatrix}$$

The resulting load in cross-section **z** is given by matrix operation

$$\mathbf{Z}_{\mathbf{r}} = \mathbf{Z}_{\mathbf{rs}} + \mathbf{T}^{\mathbf{s}}_{\mathbf{v}_r} . \mathbf{Z}_{\mathbf{vs}}$$

Conclusion

The main advantages of the described solution are as follows: the most work — difficult and time-consuming computations are done only once and the majority of matrixes is independent of the loading case and include simple geometrical parameters. The method can also be applied to other parts of an aeroplane, especially tail units, fuselage and other types of loading. The method described in this paper was successfully applied in the CAE system to aeroplane loading computation, named SAVLE, which was used in the Czech aircraft industry during the development of several aeroplanes (L-410, L-610 commuters for 19 and 40 passengers, L-159 light combat aircraft, Ae 270 commuter for nine passengers and VUT 100 *Cobra* new generation GA aircraft). The basic conceptual scheme of the system SAVLE is shown in Fig. 5 and the example of resulting shear forces diagram on L-610 commuter wing is on Fig 4.

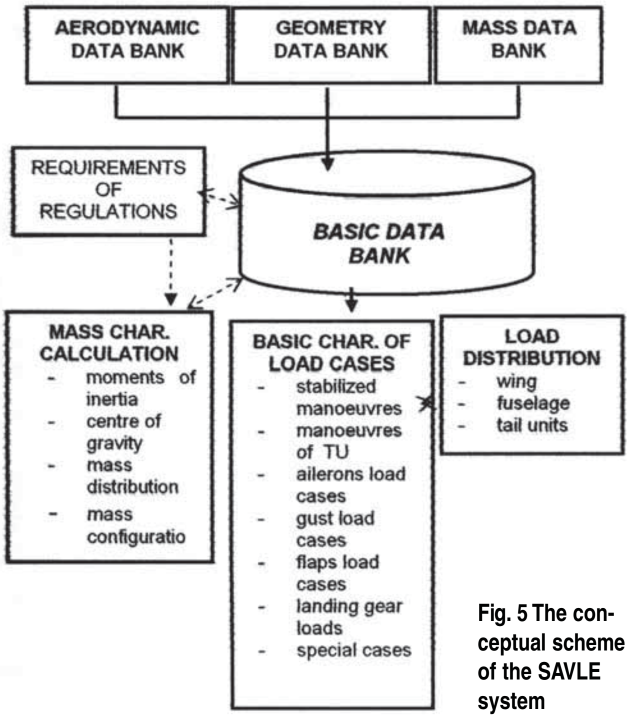

Fig. 5 The conceptual scheme of the SAVLE system

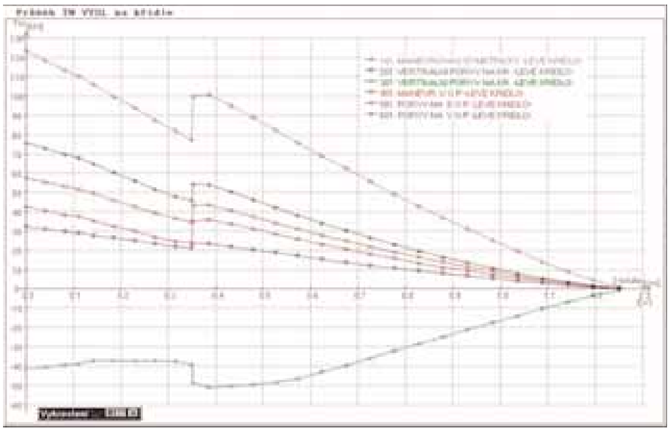

Fig. 4 The resulting shear forces diagram for L-610 commuter

References

[1] Chun-Yung Niu, M.: *Airframe Structural Design*; Lockheed Aeronautical Systems Company, Conmilit Press Ltd., Los Angeles, California, 1988

[2] Pistek A., Bohm R, Gregr O, Kahanek V.: *Pevnost a zivotnost letadel I*, VUT v Brne, Brno, 1988

[3] Pistek A.: *Automation of Load Calculation*, VUT v Brne, Brno, 1993

[4] Pistek A.: *Optimalizace leteckych konstrukci s vyuzitim MKP*; Doctoral thesis, Brno, 1980

[5] Hlinka J, Vanek F.: *Glauert III*; Institute of Aerospace Engineering, VUT Brno, 2000

Environmental Control Systems of Airplanes and Helicopters

Klimatizační systémy letounů a vrtulníků

Ing. Petr Lindovský / První Brněnská Strojírna (PBS), Velká Bíteš

The authors present the past and current status of the manufacture and development of aircraft air-conditioning systems.

Článek popisuje historii a současný stav vývoje a výroby klimatizačních systémů pro letouny a vrtulníky v První brněnské strojírně Velká Bíteš, a.s.

Keywords: air-conditioning systems, manufacture, development, history, current status.

Introduction

The Aircraft Technique Division of the Czech Company Prvni Brnenska Strojirna Velka Bites (further referred to as PBS) is a well established manufacturer of aircraft equipment used by both domestic and foreign users. The major equipment line includes main engine starters (small jet engines, auxiliary power units APUs, air starters) and environmental control systems (ECS).

This article focuses on ECSs designed for the following aircraft: jets L-39, L-59, L-159A manufactured by Aero Vodochody, ECSs produced in series for the Chinese plane K8, the development of air-condition units designed for Czech planes L-159B and EV-55 and also for Russian helicopters Mi-17 and ANSAT produced by Kazan Company KVZ, and Mi-171 by Ulan-Ude Helicopter Company UUAZ.

ECS working principle in general

ECS working principle is based upon conditioning of the air tapped from low pressure- or high pressure compressor bleed (max. pressure 1.4 MPa, max. temperature 430 degrees Centigrade) to obtain air parameters needed to heating or cooling the cockpit.

The bleed air passes through a closing valve or a precooler (in case the input air temperature is too high), air filter and flow limiter to the heat exchanger to be cooled down to a temperature of around 50 degree centigrade. The cooling medium in the exchanger is air from the ambient atmosphere, which is sucked in by a turbocooler blower wheel mounted with turbine wheel on the common shaft. The cooled air goes from the exchanger to the turbocooler turbine where its temperature drops down to -30 degree centigrade due to expansion. The turbine generated power is used to drive the blower. The turbine revolutions range mostly between 40,000 and 60,000 rpm. The warm air is by-passed past the turbine to maintain the turbine output temperature at 0 to 6 degree centigrade in order to avoid the system's freezing. The turbine output air comes to a water separator to reduce the air humidity and by adding some warm air, the air mixture gets the right temperature for the flight deck air-conditioning. Adding hot air is through regulating valves that are controlled by electric or pneumatic thermostats and a temperature selector placed in the cabin. The maximum air temperature coming into the cabin is watched by a limiting thermostat. In the cabin the air is distributed by pipes, air showers and nozzles.

The L-39 ECS

The ECS development designed for L-39 started in 1967 and Aero Vodochody company took the delivery of the first 11 sets in 1972. The set contained particular equipment including a turbocooling unit (turbocooler and heat exchanger), water separators, slide valves with electric motors, flow limiters, overpressure regulator and air shower. ECS regulation is controlled by electric circuits (maintaining the preset cockpit temperature) and the amount of air supplied is watched by a flow limiter. As the electric regulation of the air temperature is not much stable, the pneumatic air temperature control has been used for upgraded ECSs.

Some 4,500 ECS sets have been manufactured at PBS for these aircraft.

The L-59 ECS

1980 saw the beginning of developing new ECSs designed for the L-59 jet. As the bleed air parameters tapped from the engine had been altered, it was necessary to reduce the cockpit air temperature using a precooler.

To control the cockpit temperature, pneumatic regulation has been used the principle of which is controlling of by-pass valves by the controlling air. Its pressure is maintained by relieving pneumatic thermostats according to system limiting temperatures, cockpit temperature, and the temperature set by the pilot (temperature selector). The advantage of this solution is step-by-step regulation and the possibility of maintaining the cockpit pre-set temperature exactly. However, the pneumatic control instruments are very sensitive and their production tolerances must be very narrow.

With the production started in 1982, a total of 100 ECS sets have been manufactured.

The L-159A ECS

1995 saw the beginning of developing ECSs designed for the L-159A. Some older equipment was upgraded to Aero Vodochody requirements, others were newly designed. A new precooler was designed that was combined with other functions (cockpit - deicing). Pneumatic control is used in this case.

Seventy two complete ECS sets have been manufactured and delivered for the L-159A jet.

The K8 ECS

When the L-159 ECS deliveries had come to an end, there was a general recession in this product line in the Czech Republic, so PBS started to offer their systems to other potential customers.

In 2003 a contract was concluded with a Chinese customer to develop and supply ECS for the K8 trainer aircraft.

The main distinctive feature of this system is that most air-condition apparatuses are integrated into one unit (see Fig. 1).

Fig. 1 — ECS for the Chinese K8 aircraft

Based on the customer requirements to take out ECS air both from the high pressure- and low pressure compressors and with regard to the engine's altitude bleed characteristics, new equipment had to be designed. Switching from high pressure bleed to low pressure bleed is effected up to an altitude of 5,000 m with a pneumatic regulating valve depending on bleed parameters and valve output pressure. At altitudes above 5,000m, the three-way valve's altitude sensor switches the regulating valve control to the high pressure bleed, making it possible to employ its higher parameters at lower engine regimes. At maximum engine power solely the low pressure bleed is always applied. The NACA input is applied to conduct cooling air to the heat exchanger.

A new type of water separator featuring higher separation capacity has been developed to improve the quality of cockpit air.

Further, the system features a de-fog regulation circuit that makes it possible to immediately supply hot air to the canopy in case it is misty.

The amount of the air supplied to the cockpit is controlled by regulating valve in the case of high pressure bleed, and by a flow limiter for low pressure bleed.

About 100 ECS sets have been delivered to the Chinese customer so far.

The L-159B ECS

This ECS is derived from the L-159A ECS, so some equipment features commonality. Based on Aero Vodochody requirements, the pre-coolers' temperature control and OBIGGS system are modified as thermostats work depending on the regulating valve and flaps.

The second development stage concerns the modification of the turbocooling unit consisting of a larger volume of air coming to the cabin in extreme conditions in places of potential customers. This modification also calls for a new flow limiter for higher flow rates.

A new water separator with higher separation power is used as well.

			ECS L-39	ECS L-59	ECS L-159A	ECS K8	ECS L-159B
Max. inlet pressure	High pressure compressor	MPa	0,95	1,2	1,4	1,4	1,4
	Low pressure compressor	MPa	-	-	-	0,6	-
Max. inlet temperature	High pressure compressor	°C	350	430	430	430	430
	Low pressure compressor	°C	-	-	-	280	-
Heating capacity		kW	14.0	14.0	14.0	min.14.0	max.16.8
Cooling capacity		kW	2.8	2.8	2.8	min.2.8	max.3.3
Air flow rate		kg/h	max.500	max.500	max.500	min.500	max.600

Table 1 — ECS Basic Characteristics for Aircraft

ECS for the helicopters of Mi-17 family from KVZ and those of Mi-171 family from UUAZ

All ECSs manufactured so far work with the bleed air that is tapped from compressors of aircraft's main engines. If the quantity of bleed air approaches the maximum allowable amount, the engines have problems related to growing exhaust gases temperature before the turbine. Another disadvantage of the current systems is that at least one main engine must be in operation. To remove these disadvantages, it has been suggested using compressed air from the APU, which is also a PBS product and is installed on all airplanes and helicopters to which PBS delivers ECS. Based upon this idea, the PBS's Project and Development Division carried out a feasibility study in 2000 on the use of ECS combined with the APU air source.

In 2001 an agreement with Kazan Helicopter Comp (KVZ) was made to develop an ECS for the Mi-17 helicopter and its versions using air taken from APU *Saphire* 5K/G-MI, which PBS designed and delivered in series for this helicopter. Once all the ECS function requirements had been cleared, calculation of heat balance in both helicopter cabins was performed taking into account the helicopter's flight envelope and environmental comfort in the cockpit and passenger cabin. Based upon the calculation heat and/or cooling power was determined and parts of the system were modified or newly designed such as turbine, blower and outlet duct, heat exchanger, water separator, closing and regulating valves.

Work Principle

The system works on the principle of cooling the compressed air taken from APU *Saphire* 5K/G-MI, which is part of the Mi-17 helicopter system. The air comes to an inlet filter (13), see Fig.2. The system starts or stops by a closing valve (13), which is in off position before start. The valve shuts if there is a malfunction in the system.

Past the closing valve (8), the air pipeline is divided in two circuits:

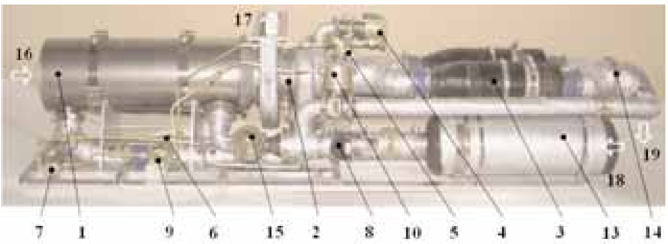

Fig. 2 — Environmental control system for the Mi-17 type of helicopter and its derivatives

Air Cooling Circuit

It consists of heat exchanger (1), turbocooling unit (2), water separator (3) and apparatus to control outlet turbocooling temperature, i.e. input filter (7), pressure reducing valve (6), regulating valve (4) and thermostat with filter (5).

The air coming to heat exchanger (1) is first cooled by air sucked from ambient atmosphere and after being cooled it expands in turbocooler unit. Thermostat (5) and pressure reducing valve (4) control the turbocooling unit outlet temperature to 0 - 6 centigrades to prevent system from freezing.

The water from separators (3) passes through an ejector which is driven by pressure air taken from heat exchanger outlet section (1), and then goes to heat exchanger air intake. Through water evaporation in suction of the heat exchanger the efficiency of the latter increases, particularly in extreme humidity conditions.

Temperature Control Circuit in Cabin

It consists of regulating valves (10), (15), thermostats with filter (11), (12) and a pressure reduction valve (9). The cabin is heated or cooled depending on its temperature. When the cabin is cooled, i.e. its temperature is above 22 centigrade (upper limit of pre-set temperature 20 +/-2° C), the thermostat with filter lets more controlling air pass. In membrane space of the regulating valves (10) and (15) the overpressure of controlling air decreases, causing regulating valve (15) to open and regulating valve (10) to shut. Most air flows to the cooling circuit and the air with a resulting temperature of 0 to 6° C flows into the cabin. The cabin temperature is getting lower due to the cold air supply.

When the cabin is heated, i.e. its temperature is below 18 centigrade (low limit of pre-set temperature 20 +/-2° C), the thermostat with filter (12) stops the flow of controlling air. In membrane space of the regulating valves (10) and (15) the overpressure of controlling air increases, causing regulating valve (15) to close and regulating valve (10) to open. Most of the air goes directly into the cabin. Limiting thermostat (11) starts closing regulating valve (10) and opening regulating valve (15) so that the maximum permissible temperature of air coming into the cabin is not exceeded.

The check valve (14) prevents warm air from flowing from regulating valve (10) to separators (3) and turbocooling unit (2). Controlling air for pneumatic control equipment is taken out past the closing valve (8).

Laboratory tests of an ECS prototype began at PBS in 2005, first simulating bleed air by taking air out of the lab's pressure air supply, then with the help of APU *Saphire* 5K/G-MI. The tests have verified that the system works properly and the pneumatic control is capable of switching from cooling to heating and vice versa. After finishing the first tests there followed detailed trials of turbine parameters, blower, blower outlet, and heat exchanger. The trials serve for calculation of how the system works in non-designed points and also for quality evaluation of particular parts and further improvements.

April 2006 saw ground tests at the Přerov air base. The power and functioning of the ECS were tested in heating and cooling regimes concerning the entire helicopter or its cockpit only.

At present this ECS is being modified to be used on Mi-171š helicopters where installation requirements are different. The Mi-171š helicopters are operated by the Czech Air Force.

ECS for ANSAT Helicopter

Following talks with the KVZ company, PBS was asked to develop an ECS for the small helicopter type ANSAT powered by two PW-207K engines.

PBS has designed and manufactured a functional sample of ECS with required air parameters taken from the two engines and made successful laboratory trials.

The functional sample was delivered to KVZ in 2005 to be flight- and ground-tested on the helicopter. The tests are to be taken in the near future.

		ECS Mi-17	ECS ANSAT
Maximum inlet pressure		430 kPa	600 kPa
Maximum inlet temperature		210 °C	330 °C
Heating capacity		max. 58.4 kW	12.6 kW
Cooling capacity		max. 7.5 kW	2.5 kW
Air flow rate	Heating	1 600 kg/hour	~ 450 kg/hour
	Cooling	900 kg/hour	

Table 2 Basic Characteristics of ECS for Helicopters

ECS for the EV-55 airplane

PBS has collaborated with the EVEKTOR Company since 2005 on developing ECS heating and air conditioning components for the new EV-55 airplane to provide sufficient comfort and fresh air supply to the flight deck and the passenger cabin. The system's drawing is depicted in Fig. 3.

Description of Heating System

The hot air taken from compressors of the two engines (1) goes through a compensation loop (2), closing valve (3), and pipeline (4) to the wing centre section where the left hand side and right hand side branches of hot air are connected by merger (6). There are check valves (5) placed before connection of both branches. Then there is a pressure air branch of pneumatic de-icing followed by a flow limiter which assures sufficient overpressure in the de-icing system. Behind the flow limiter is regulating valve (7) that controls air supply to the mixer. From regulating valve the hot air comes through compensators (8) to mixer (10) where it is mixed with cold atmospheric air. The latter is brought to the mixer by NACA air intake (11) which is fitted with a flap valve and drainage. The mixed air then passes through silencer (12) to the redistribution valve pilots-passengers (13) where the heating air is divided into the flight deck and the passenger cabin. In the passenger cabin the air is distributed by means of heating lines (14) on the cabin left and right sides. A hose pipe serves to deliver heating air to the flight deck. In the cockpit central section is a flap valve "legs-window" (15) allowing to supply air towards either pilots' legs or windscreen (17) and side showers (16). The pilots can individually control the amount of leg warm air. The cabin temperature is controlled by an automatic control unit, which is being developed by the MESIT Co. Ltd. The unit picks up the cabin temperature with a sensor placed in the cabin and the mixed air temperature past the silencer with a sensor placed in one of the branches. Based upon data from temperature sensors and the temperature set on the controller in the cockpit, the unit controls regulating valve (7) and checks hot air supply to the mixer to keep the chosen temperature. The unit also ensures that the temperature past the mixer does not exceed 100° C and the air temperature coming to the cabin is not higher than 80° C.

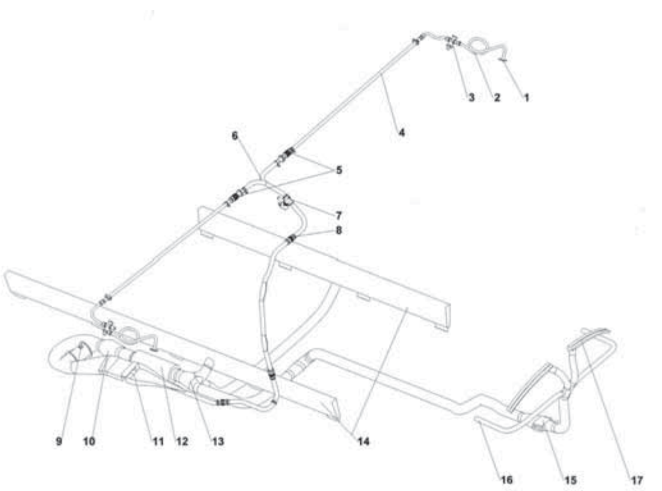

Fig. 3 — Environmental Control System for EV-55 (Courtesy EVEKTOR company)

Description of Ventilation System

The ventilation system is created with the help of the heating system. In the cold ambient, the supply of fresh outside air passes through the heating system so that warm air is delivered. In the warm ambient, the cabin ventilation is implemented through the heating system in which hot air supply from the compressor is closed. When on the ground, the heating system works with a bypass fan (9). Outside air for air showers is brought in by left and right vents in the cabin ceiling. Each vent has its own NACA-intake placed in the upper front part of the fuselage. There is a bypass fan in each vent which ensures the outside air supply when the plane is on the ground. The cockpit is vented by means of individual showers in pilots' dashboard. Air to these showers comes through air intakes in front of the head windows.

PBS participates in the design and optimal arrangement of pressure air supply from engines, heating air distribution to the cockpit and the passenger cabin (including re-distribution flap valves), check valves (5), regulating valve (7), mixer (10), and noise silencer (12). PBS is also responsible for the design of a test stand and functional measurement of the whole system.

ECS EV-55		
Maximum inlet pressure		600 kPa, abs.
Maximum inlet temperature		265 °C
Heating capacity		max. 7.2 kW
Air flow rate	for cabin inlet temperature 80°C	max. 470 kg/hour
	for cabin inlet temperature 60°C	max. 740 kg/hour

Table 3 — Basic characteristics of EV-55 ECS

Material Sciences in Microgravity: TITUS MPP Facility

Tool for the Crystal Growth and Solidification on Board the International Space Station (ISS)

Experimentální výzkum růstu krystalů v podmínkách mikrogravitace na palubě mezinárodní kosmické stanice ISS

Dipl. Ing. Čestmír Bárta Jr., PhD, Dipl. Ing. Čestmír Bárta, PhD, Dipl. Ing. Martin Bernas, PhD / BBT-Materials Processing, Crystal Science & Technology Institute, Prague; Dr. Reinhard Roestel / http://www.temperaturmessung.biz; Dr. Frank Winkler / Humboldt-Universität zu Berlin, Institut für Informatik

The long-term microgravity represents an important parameter and powerful tool for crystal growth and material science experiments. The International Space Station (ISS) brings new chances and challenges for the research in this field. The correct preparation and realisation of such material science and technological experiments in microgravity call for specific devices and instruments enabling to create suitable conditions to obtain results which can effectively contribute to solve actual problems and challenges. On the contrary, improperly prepared experiments can provide results which distort the reality and possibilities of this field of science and often damage a reputation of Science in general.

The paper presents a TITUS MPP Facility (Tubular Furnace with Integrated Thermal Analysis under Space Conditions — Multi-Purpose Platform) which can meet all the necessary requirements. It has been developed and manufactured by the team of scientists and other specialists within the BBT-Materials Processing, Crystal Science & Technology Institute, Prague, Czech Republic (BBT) for the DLR-MUSC (German Aerospace Center - Microgravity User's Support Center) and ESA (European Space Agency) in close cooperation with Humboldt University in Berlin and Kayser-Threde (Germany). The modular concept of the TITUS MPP Facility enables its exploitation by a broad international community of scientists and technologists as it was in case of our preceding generations of the facilities (CSK-1C and TITUS) on board the space station MIR (Figs. 1 to 5).

Dlouhodobá mikrogravitace představuje důležitý parametr a mocný nástroj pro experimenty s růstem krystalů a pro materiálové vědy. Mezinárodní vesmírná stanice ISS přináší nové šance a výzvy pro výzkum na tomto poli. Korektní příprava a realizace takových materiálových vědeckých a technologických experimentů vyžaduje specifická zařízení a přístroje umožňující vytvořit vhodné podmínky k získání výsledků, které mohou efektivně přispět k řešení aktuálních problémů a výzev. Naopak, nesprávně nebo nevhodně připravené experimenty mohou poskytnout zavádějící či mylné výsledky, které zkreslují realitu a možnosti v této oblasti vědy a často poškozují reputaci Vědy jako takové.

V tomto článku je představeno zařízení TITUS MPP Facility (Tubular Furnace with Integrated Thermal Analysis under Space Conditions — Multi-Purpose Platform, tedy: Trubková pec s integrovanou termickou analýzou v kosmických podmínkách — Mnohoúčelová platforma), která splňuje všechny potřebné požadavky. Zařízení bylo vyvinuto a postaveno týmem vědců a dalších specialistů ve firmě BBT-Materials Processing, Crystal Science & Technology Institute, Praha (BBT) pro DLR-MUSC (Německé centrum pro letectví a kosmonautiku - German Aerospace Center - Microgravity User's Support Center) a pro ESA (Evropská kosmická agentura - European Space Agency) v úzké spolupráci s Humboldtovou Universitou v Berlíně a německou firmou Kayser-Threde. Modulární koncept zařízení TITUS MPP Facility umožňuje jeho využití širokou mezinárodní komunitou vědců a technologů, jako tomu bylo v případě našich předchozích generací zařízení (CSK-1C a TITUS) na palubě kosmické stanice MIR (obr. 1 až 5).

Keywords: Materials science, Microgravity, Crystal growth, Solidification, Eutectics, Phase equilibria, Supersaturated solutions, Undercooling, Titus.

---

1. Introduction

The crystal growth and material sciences under microgravity have a more than 30-year-tradition. During the time a range of interesting discoveries and important results have been gained and some progressive technological procedures of preparation of materials under microgravity have been developed.

From the viewpoint of crystal growth and material sciences, the long-term microgravity represents the most important parameter of space environment and a powerful and irreplaceable unique tool which enables study of fluids in an absence of gravity-induced convection and sedimentation and gradients of hydrostatic pressure. Thus, it also creates presumptions for the formation of extraordinary deep undercooling of liquids and for the volume solidification and crystallization under extremely non-equilibrium conditions (undercooling, supersaturation, significant influence of surface tension and diffusion, etc.) and enables better understanding of the influence of gravity segregation on the homogeneity of dopants in the crystal. Based on the results it will be possible to better understand the rules of crystallization and solidification processes and exploit them for a simulation of conditions in ground laboratories for the development of new technologically interesting materials with required applicable properties and features.

Fundamental results were obtained in the field of mass and heat transfer, namely deeper understanding of rules of a non-gravitational convection of fluids as a result of the gradient of surface tension (”Marangoni convection“) or processes which occur during the solidification. The course of nucleation and crystal growth processes is specifically different in microgravity. It was found that in optimal exploitation of microgravity conditions it is possible to prepare materials with specifically different composition, structure, microtexture and consequently with modified physical properties and features. Under microgravity, surface tension and diffusion can play a significant role as a driving force of a mass transport. It is also possible (in selected materials) to reduce heat transfer to conduction only. The knowledge of these phenomena (in connection with a possibility to avoid sedimentation and convection) opens interesting perspectives in space technology in the field of development of new technical materials and remedies. But, a main value of the crystal growth and material science experiments in space should be considered as a basic source of information for the verification of the theoretical models and an improvement and optimisation of ground technological procedures, technical features and quality of crystals, alloys and other materials produced on Earth.

So far, several applicable interesting technological procedures using microgravity conditions have been already developed:

- ◆ Thanks to extraordinary efficiency of zone melting techniques (as a consequence of suppressed convection) there is a possibility to prepare materials of extremely high chemical purity which are necessary for a production of volume semiconductors and optical materials of very high quality.
- ◆ For the same reasons it is possible to produce serum and vaccines of extra purity (using isotachophoresis and other techniques) without undesirable side-effects.

Fig. 1 — CSK1-C space furnace with the astronauts Pedro Duque (Spain) and Ulf Merbold (Germany) — Project EuroMIR ‘94 [Photo DLR]

Fig. 2 — CSK1-C space furnace with the German astronaut Klaus-Dieter Flade — Project MIR ’92 [Photo DLR]

- ◆ Growth of large single crystals of mixed semiconductors and proteins and other biological substances has been proved. Their high quality is practically not accessible under normal gravity.
- ◆ New technological procedures of preparation of alloys have also been successfully proved, namely for aircraft and automotive industries, e.g. mouldless casting of bulky casts and new casting procedures using a Marangoni convection in combination with an absence of sedimentation (avoiding aggregation and sedimentation of fine segregated and other microparticles of additions aimed to their controlled inclusion). Using this method, aluminium based alloys have been developed suitable for self-lubricating bearings (friction decreased to 50% and wear to 10%).
- ◆ Preparation of glasses with a significantly broader extent of compositions than can be achieved on Earth (e.g. semiconductors, lasers, optical fibres).

2. ISS — New chances and challenges

Compared to the past possibilities on board MIR, the International Space Station (ISS) brings further new and better chances and challenges for the research in the field of materials processing, namely crystal growth and solidification in microgravity (higher technical level, energy sources and space capacity, human resources, etc.). ISS will enable scientists to realise sets of systematically prepared experiments using advanced customised facility as it is common in material science laboratories on ground.

A proper preparation and realisation of such crystal growth experiments requires specific devices and instruments. The authors, based on 30-year-experience in material science and space technology [1 - 44], believe that the research equipment should meet namely the following basic requirements:

1 The facility should be equipped with a system of damping of disturbing vibrations and micro-accelerations generated on board the orbital laboratory which would enable a maximum exploitation of a unique microgravity environment to obtain proper experimental results. In addition, a magnetic damping device should minimise convection or convert a turbulent into laminar convection in fluids. It is a necessary presumption to achieve highly non-equilibrium conditions of solidification.

Fig. 3 — TITUS space facility with German astronauts Hans-Dieter Schlegel and Reinhold Ewald — Project MIR '97 [Photo DLR]

2 Based on a highly modular concept, the facility should represent a set of specialised instruments for measurements of thermodynamic and other physico-chemical gravity dependent constants under deep microgravity, in absence of convection and in a broad region of boundary conditions up to critical points of phase transitions. It should help in determination of non-equilibrium (metastable) phase diagrams and phase transitions, temperature dependencies of diffusion and distribution coefficients, effective heat conductivities, surface tensions and other basic fluid parameters. The obtained results will enable a proper and systematic selection and preparation of space experiments aimed to the development of new technologically perspective materials.

3 The facility should be equipped with a set of specialised modules for an appointment of crystallo-chemical parameters (metastable region width, growth rate, etc.), namely as a dependence on temperature, temperature gradient, critical values of vibrations, magnetic field, segregation, homogeneity of dopants, etc. The aim is to optimise conditions for the reproducible preparation of new perspective materials with required properties.

4 The facility should be able to realise model and technological experiments, namely precisely controlled temperature field in time and locally, with a high accuracy, reproducibility, reliability up to 1500-1600° C. A possibility of *in-situ* visual monitoring of the solidification process (transparent aerogel furnace) and "tele-science" are highly demanded.

5 The modular concept of the facility should cover all experimental requirements by easily exchanging or adding components for measurement, diagnosis, and operation (easy repairs and upgrades).

Under above mentioned conditions material science and technological experiments in microgravity can be performed properly and obtained results can effectively contribute to solve actual technological problems and challenges. On the other way, improperly prepared experiments can provide results which often distort reputation and possibilities of this field of science.

3. TITUS MPP Facility

The TITUS MPP Facility (Tubular Furnace with Integrated Thermal Analysis under Space Conditions — Multi-Purpose Platform) is the latest development — 4th generation of our space furnaces. It can meet all the above mentioned requirements. It has been developed by the Czech-German team of scientists (BBT-Materials Processing, DLR-MUSC, Humboldt University). The facility is designed to supplement other facilities planned for the ISS and has plain interfaces to the station, i.e. only power supply and telemetry will be required. The application of a strictly modular concept with components easily to be exchanged for repair or up-grading of the facility to the latest state of development enables its exploitation by a broad international community of scientists and technologists (for details see: http://bbt.mysteria.cz).

The TITUS MPP Facility is designed for materials experiments dedicated to e.g. solidification processes, crystal growth, diffusion and physical chemistry. The following experimentation techniques can be utilised: Bridgman, travelling heater method, gradient freezing, zone melting, isothermal processing (annealing, preparation of glasses, etc.), condensation and chemical transport, differential thermal analysis (DTA), directio-

Fig. 4 — TITUS space facility on board the MIR space station with the French astronaut Jean-Pierre Haigeneré — Project MIR '99 - PERSEUS [Photo CNES, France]

Fig. 8 – TITUS MPP – Bread-board model BM-1

Editorial note: Further numbered illustrations to this article mentioned in text are printed in colour on third inner cover page.

nal solidification of multicomponent melts, polycrystals, alloys, sublimation growth and chemical vapour transport reactions, etc.

In addition, the facility enables to work under deep microgravity conditions (using the special damping system) which enables to reach extremely non-equilibrium conditions in fluids and to appoint the particular thermodynamic parameters (heat transfer, etc.).

Starting with CSK-1C furnace on board MIR (Figs. 1, 2 and 5) and continuing with TITUS facility (Fig. 3) which has last been used during the French PERSEUS space mission in 1999 successfully serving two experimenters on board MIR (Fig.4, 5), TITUS MPP Facility (Figs. 6, 7, 8, 9 and 10) is the latest development in a series of furnaces.

Based on the long-term experience gained from the operation on board the space station MIR a modular concept has been developed considering the specific requirements of long-term operation in a space station environment. These operational conditions require the improvement of overall reliability and lifetime, in case of failures components shall be easily exchan-

Characteristics of the TITUS MPP Facility — basic configuration:

Dimensions:

Volume 1200 x 300 x 400 mm, Mass 50-65 kg

Mains: Voltage 28 2 V DC, Max. power 700 W, Average power 400 W

Heater: 9 (7 narrow, 2 wide) individually controlled zones (heated length: 268 mm, inner dia: 16.5 mm)

Max. temperature: 1300° C (optionally 1500-1600° C)

Temperature range: 100 to 1300° C

Temperature resolution: ≤ 0.1 K

Temperature stability: ≤ ±0.15 K

Temperature setting accuracy: ± 2.5 K

Sample:

Useable sample volume approx. 250 x ∅ 25 mm

Feeding velocity:
— for experiments: 0.01 to 20.8 mm/h
— for replacement: 1, 2, 3, 4, 5, 40 and 600 mm/min

Feeding length: 480 mm

Positioning accuracy: < ± 0.01 mm

Max. Temperature: 1250° C (optionally 1500° C)

Temperature gradient: 30-50 K/cm

Gravitation — 3-axis measurement:

Frequency range of measurement: 0.01 … 10 Hz

Measuring frequency (selectable): 1/60 … 200 Hz

Measuring resolution: 5 µg

Temperature:

10 temperature channels (up to 40 thermocouples)

Measuring frequency (selectable): 0.1 - 10 Hz

Measuring resolution:
— at frequency 0.1-1 Hz: ≤ 0,0025 K
— at frequency 10 Hz: ≤ 0,01 K

Absolute accuracy: ≤ ± 1 K

Temperature variation along the sample main axis for isothermal conditions: ≤ 1 K (at 100 mm length

Others:

— high precision temperature measurement and DTA
— damping system to reduce board effects (vibrations and micro-accelerations)
— hermetically closed working space enabling processing of toxic materials
— optional magazine for 20 cartridges for the automatic processing of set of samples
— dedicated external computer of standard laptop type operating as 'master' of the facility 'slave'
— the facility and providing data transfer by the station telemetry system
— software supporting the crew by displaying the operating procedures synchronously to the status of the facility

The introduction of the following diagnosis methods is under consideration:

— determination of solidification front position by electrical resistance measurement
— ultra-sonic analysis of solidification process
— marking of phase boundary
— high precision temperature measurement as calorimetry, heat conductivity and thermodynamic constants measurements.
— optical fibre thermometry (accufibre)
— extension of the sample diameter up to diametre 25 mm (optionally 40 mm)
— rotating magnetic field
— transparent furnace unit with in-situ monitoring (CCD camera)
— opening the field of fluid physics to experimentation by introducing a low-temperature control module.

Fig. 9 — TITUS MPP - Bread-board model BM-2 (furnace module)

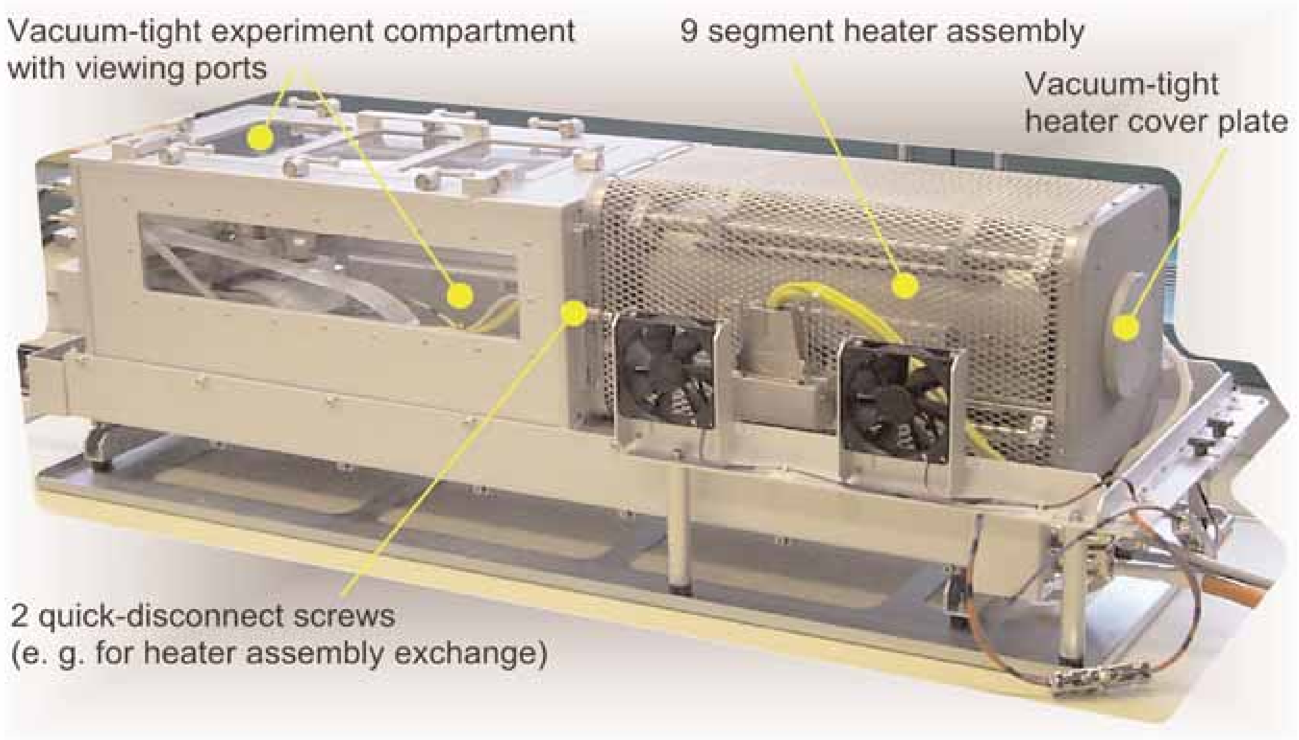

ged and replaced by spare parts. Additionally, new experimental and diagnostic methods will be introduced to keep experimentation at the state of the art and to make space experimentation more attractive for scientists.

The TITUS MPP Facility is expected to be used for the study of model and experimental materials important namely for semiconductors, detectors, optics (crystals and glasses), sensors of electro-magnetic radiation, recording and processing of information, pharmaceutical industry (polymers, proteins), automotive and aerospace industries (construction materials as composites and alloys based on titanium, aluminium, iron etc.), development of new types of materials (alloys) for self-lubricating bearing, etc. A variety of eutectic and peri-eutectic alloys, glasses and organic compounds with a low melting (sublimating) point and selected values of density, viscosity, pressure tension and other physico-chemical parameters will be used as model fluids for a study of convection and solidification processes. Specific materials will be currently selected for the experiments based on actual needs and results (e.g. metallic foams, composite materials with solid particles or controlled gaseous inclusions, etc.).

A successful systematic work on board the orbital laboratory for crystal growth and material sciences expects also similar ground laboratory, indeed, where a proper ground preparation of space experiments and parallel comparable and reference experiments and their scientific evaluation would be performed.

4. Conclusions

The TITUS MPP Facility as the last facility in the row of successful predecessors is designed to be utilised on board ISS. The basic version comprises electronics for temperature measurement and control, acceleration measurement, and data acquisition, pre-evaluation, storage and telemetry. The high versatility is achieved by the modular design, which allows the adaptation to a wide range of experimental requirements. Due to easily exchangeable components maintenance and repair require only low effort, adding components allows upgrading even on station. TITUS MPP Facility will contribute to make space experimentation more attractive to scientists and to open new fields of research.

Fig. 10 — TITUS MPP - Bread-board model BM-2 (electronics module)

5. Acknowledgements

The financial supports of the Ministry of Education of the Czech Republic under the program *KONTAKT* (ME308/1999) and *ESA-PRODEX* (14572/00/NL/Sfe(IC)) are greatly appreciated.

References

[1] Barta, C., Stourac, L., Trnka, J., Triska, A., Zemlicka, J., Barmin, J.B., Iljin, A.A., Ochotin, A.S., Zubrickij, I.A.: *Experiment MORAVA on Board the Salyut 6: I. Crystallization of Lead Chloride from Eutectic Solution in $PbCl_2$ - AgCl and $PbCl_2$-CuCl Systems*; 29th Int. Astronautical Congress, Dubrovnik, Oct 1978, Part I, I.N./26/, p. 162, Peace and Human Progress, Pergamon Press,1979, pp. 391

[2] Barta, C., Trnka, J., Triska, A., Khhrjapov, V.I., Ochotin, A.S., Zubrickij, I.A.: *Experiment MORAVA on Board the Salyut 6: II. Crystallization of Lead Chloride and Mercurous Bromide from Eutectic Solutions*; Proc. of 3rd European Symp. on Material Science in Space, Grenoble, 24-27 Apr 1979, ESA SP-142, June 1979, pp. 215

[3] Barta, C., Triska, A., Ochotin, A.A.: *Czechoslovak Preliminary Program of Material Research in Space*; Proc. of 3rd European Symp. on Material Science in Space, Grenoble, 24-27 April 1979, ESA SP-142, Jun 1979, pp. 213

[4] Barta, C., Triska, A.: *Actual Problems and Perspectives of Space Technology*; 6th Conf. of Czechoslovak Physics, Ostrava, 27-31 Aug 1979, Proc. Part 2., CC-85-115, published by JCSMF Ostrava

[5] Barta, C., Stourac, L., Triska, A., Kocka, J., Zavetova, M., Ochotin, A.S.: *Influence of Microgravity on the Physical and Crystallochemical Properties of Glassy Ge-S-Sb*; Proc. of the 8th Int. Conf. Amorphous and Liquid Semiconductors, Cambridge/Boston, USA, Aug 1979, J. Non-Crystalline Solids 35 and 36, 1980, pp. 1239

[6] Barta, C., Stourac, L., Trnka, J., Triska, A., Khrjapov, V.T., Ochotin, A.S, Tatarin, V.A., Zubrickij I.A.: *Experiment MORAVA on Board the Salyut 6: III. The Influence of Microgravity during Solidification of Glassy Ge25S55Sb20 on its Ability for Recrystallization*; 30th Congress of the Int. Astronautical Federation, Munich (Germany), Sep 1979, Acta Astronautica 6/7, 1980, pp. 441, Part II, IN(25)215-219

[7] Barta, C., Triska, A., Trnka, J.: *Facility for Study of Processes during Solidification and Crystallization of Materials under Zero Gravity Conditions*; 32nd Int. Astronautical Congress of the IAF, Rome, Italy, 5-12 Sep 1981, Adv. Space Res 1, 1981, pp. 121

[8] Barta, C., Trnka, J., Triska, A.: *To Some Czechoslovak Experiments Selected in the Field of Materials Research under Zero Gravity Conditions*; Proc. of the Topical Meeting of COSPAR Interdisciplinary Scientific Commission, Budapest, June 1980, Adv. Space Res., Vol. 1, pp. 65-68, COSPAR, 1981.

[9] Chvoj, Z., Barta, C.: *Remark on the Influence of Gravitation on the Solidification of the Binary Systems*; Czech. J. Phys., B 36, 1986, pp.868

[10] Barta, C., Trnka, J., Triska, A., Rysava, N.: *A New Module for the CSK-1 Crystallizer: Thermographic DTA Probe for the Study of Metastable Phase Equilibria under Microgravity Conditions*; Proc. of the 27th COSPAR Meeting, Espoo, Finland, 18-29 Jul 1988, Adv. Space Res., Vol. 8., No. 12, 1988, pp.140

[11] Barta, C., Fendrych, F., Krcova, E., Trnka, J., Triska, A.: *Directional Solidification of Complex-forming Eutectic Melts of the $PbCl_2$-AgCl Dielectric System under Conditions of Zero, Normal and Increased Gravity*; Proc. of the 27th COSPAR Meeting, Espoo, Finland, 18-29 Jul 1988, Adv. Space Res., Vol. 8, No. 12, 1988, pp. 167

[12] Barta, C., Kuhl, R., Trnka, J., Triska, A., Regel, L.L.: *Technological Properties of CSK-1 Crystallizer for Material Research in Space*; Crystal Research and Technology, 24, 1989, pp. 717

[13] Barta, C., Triska, A., Fendrych, F., Krcova, E.: *Directiona Solidification of the $PbCl_2$-AgCl Eutectic System under Various Gravitational Conditions*, Proc. of the 7th European Symp. on Material and Fluid Sciences in Microgravity, 10-15 Sep 1989, Oxford, Izd. Nauk 44, pp. 179

[14] Barta, C., Fendrych, F., Recker, K., Wallrafen, F.: *Influence of Crystallization Conditions on the Microstructure of the Directionally Solidified Eutectic of the MgF_2CaF_2 system*, Cryst. Res. Technol., 25, 1990, pp. 1287-1298

[15] Bewersdorff, G. P., Goerler, G.P., Otto, G., Wittmann, K., Barta, C., Fendrych, F., Triska, A.: *Solidification of Silver-Germanium Alloys in an Amorphous Matrix Aboard the Space Station MIR*; Acta Astronautica, Vol. 29, No. 7, 1993, pp. 547-552

[16] Goerler, G.P., Otto, G., Wittmann, K., Barta, C., Barta Jr., C., Triska, A., Fendrych, F.: *Analysis of Silver-Germanium Alloys Solidified from the Undercooled Melt in Microgravity*; 44th Congres of the IAF, Oct 16-22, 1993, Graz, Austria (IAF-93-J.4.291)

[17] Goerler, G.P., Otto, G. Wittmann, K., Barta, C., Barta Jr., C., Triska, A., Fendrych, F.: *Analysis of Silver-Germanium Alloys Solidified from the Undercooled Melt in Microgravity*; Microgravity Quarterly, Vol. 4, No. 3, July 1994

[18] Vojtech, D., Holecek, S., Barta, C., Barta Jr., C.: *The Ag-Ge Alloy Crystallization in Microgravity Conditions*; Proc. Conf. Pokroky fyzikalni metalurgie, 1996, Brno, pp. 99-102

[19] Vojtech, D., Holecek, S., Barta, C., Barta jr., C, Goerler, G.P., Otto, G., Wittmann, K.: *Crystallization of Silver-Germanium Alloys under Microgravity - I. Eutectic Crystalization in Hypoeutectic Alloy*; Cryst. Res. Technol., 32, 1997, 7, pp. 973-981

[20] Vojtech, D., Holecek, S., Barta, C., Barta jr., C., Otto, G., Gorler, G., Wittmann, K., Rostel, R.: *The influence of Convection on Non-Equilibrium Solidification of Silver-Germanium Alloys*; Proc. 9th Int. Metallurgy and Materials Congress, Istanbul 1997, pp. 1525-1530

[21] Vojtech, D., Holecek, S., Barta, C., Barta Jr., C., Gorler, G.P., Otto, G., Wittmann, K., Rostel, R.: *Crystallization of Silver-Germanium Alloy under Microgravity Conditions*; Proc. Conf. Euromat 97, Maastricht, Vol. 1, pp. 455-458, 1997

[22] Vojtech, D., Holecek, S., Barta, C., Barta Jr., C., Goerler, G.P., Otto G., Wittmann K.: *Crystallization of Silver-Germanium Alloys under Microgravity - I. Eutectic Crystallization in Hypoeutectic Alloy*; Crystal Research and Technology, 32, 1997, pp. 973

[23] Vojtech, D., Holecek, S., Barta, C., Barta Jr., C., Goerler, G.P., Otto G., Wittmann K.: *Crystallization of Silver-Germanium Alloys under Microgravity - II. Primary Crystallization*; Crystal Research and Technology, 33, 1998, pp. 867-873

[24] Vojtech, D., Barta, C., Barta Jr., C.: *Influence of Convection on the Course of Nonequilibrium Crystallization of Anomalous Silver-Germanium Eeutectic*; Kovove materialy 36, 1998, No. 6, pp. 381-392

[25] Vojtech, D., Barta, C., Barta Jr., C.: *Influence of Transport Processes in Melt on the Dendritic Microsegregation in Ag-Ge Alloys*, Proc of Conf. Difuze a termodynamika materialu, Tri Studne, 1998, pp. 109-112

[26] Vojtech, D., Barta, C., Barta Jr., C.: *The effect of Convection on the Nucleation and Growth Stage of the Crystallization of Silver-Germanium Alloys*; Conf. Material Congress 98, Frontiers in Materials Science and Technology, Cirencester, Proc. pp. 50. (poster), 1998

[27] Vojtech, D., Barta, C., Barta Jr., C.: *Some Aspects of Non-Equilibrium Crystallization in Microgravity*; Proc. Conf. Metallography ’98, Stara Lesna, pp. 144-147 (oral), 1998.

[28] Vojtech, D., Barta, C., Barta Jr., C.: *The effect of Convection on the Nucleation Stage of Primary Crystallization of Silver-Germanium Alloys*; Proc. Conf. METAL ‘98, Vol. 1. 12-14 May, 1998, Ostrava, pp. 176-177

[29] Vojtech, D., Barta, C., Barta Jr., C.: *Some New Pieces of Knowledge on the Non-Equilibrium Crystallization of Alloys*; Proc. Conf. METAL ‘98, Vol. 4, 12-14 May, 1998, Ostrava, pp. 7-13 (oral)

[30] Vojtech, D., Barta, C., Barta Jr., C., Otto, G., Gorler, G.P., Wittmann, K.: *Non-Equilibrium Primary Crystallization in Silver-Germanium Alloy under Microgravity Conditions*; Mater. Sci. Technol., Vol. 15, 1999, pp. 1266-1272

[31] Vojtech, D., Barta, C., Barta Jr., C., Maixner, J., Hejdova, H.: *Thermal Stability of Rapidly Solidified AlFeCrSi Powders*; Proc. 7th Int. Conf. IFHT (Heat Treatment and Surface Engineering of Light Alloys), Budapest, 1999, pp. 471-3

[32] Vojtech, D., Barta, C., Barta jr., C., Serak, J.: *Metallographic Study of the Rapidly Solidified AlFeCrSi Alloys for the Elevated Temperatures Applications*; Proc. Int. Conf. Deformation and Fracture in Structural PM Materials, Piestany, 1999, Vol. 1, pp. 95-102

[33] Vojtech, D., Barta, C., Barta Jr., C.: *PM Alloys of AlFeCrSi for Applications at Elevated Temperatures*; Proc. Conf. Metallography for Industry, Mar. Lazne, 1999, p. 40

[34] Vojtech, D., Barta, C., Barta Jr., C.: *Powder Al-Alloys of AlFeCrSi for Applications at Elevated Temperatures*; Proc. Conf. Metal ‘99, Ostrava, 11-13 May, 1999, Vol. 3, pp. 59-65

[35] Vojtech, D., Barta, C., Barta Jr., C.: *The Importance of the Rapidly Solidified Al-Alloys for Applications at Elevated Temperatures*; Proc. Conf. Present Knowledge on Materials and Technological Processes at Al-Alloys Casting, Ml. Boleslav 1999, p. 95

[36] Vojtech, D., Tagijev, E., Barta, C., Barta Jr., C.: *Heat Treatment of High-Strength Al-Alloys with Improved Casting Properties*; Proc. 18th Conf. Heat Treatment of Non Ferrous Alloys and Advanced Materials, Brno 2000, p. 365.

[37] B. Bartova, D. Vojtech, C. Barta, C. Barta, Proc. 18th Conf. Heat Treatment of Non Ferrous Alloys and Advanced Materials, Brno 2000, pp. 373

[38] Barta Jr., C., Barta, C., Sestak, J., Roestel, R., Naehle, R.: *Application of DTA Technique in Material Research under Microgravity*; CCTA 8 (8th Conf. on Calorimetry and Thermal Analysis and International Symposium on Thermodynamics), Sep 3-8, 2000, Zakopane, Poland

[39] Barta Jr., C., Barta C., Sestak, J., Roestel, R., Naehle, R.: *Application of DTA Technique in Material Research under Microgravity*; ICTAC 12 (12th Int. Conf. on Thermal Analysis and Calorimetry), Aug 14-18, 2000, Copenhagen, Denmark, publ. in Abstract Book, additional poster abstracts, Mater. Sci. PII-34, p. 8

[40] Vojtech, D., Barta, C., Barta Jr., C.: *Evaluation of the Microgravity Experiment with Ag-Ge under Microgravity*; Kovove materialy (Metallic Materials) 39 (6), 2001, p. 410

[41] Vojtech, D., Serak, J., Cabalka, A., Barta, C., Barta Jr., C.: *The influence of Sr Modification on the Structure of Directionally Solidified Al-Si alloys*; Acta Metallurgica Slovaca (special issue) 1, (2001), p. 178

[42] Barta, C. jr., Barta, C., Sestak, J.: *Thermophysical Research under Microgravity (Space Laboratory TITUS)*; Proc. 3rd Int. Conf. on Intelligent Processing and Manufacturing of Materials (IPMM-2001), Jul 29 - Aug 3, 2001, Vancouver, Canada

[43] Vojtech, D., Tagiev, E., Barta, C., Barta Jr., C., Serak, J., Janda, P., Ekrt, O.: *Casting Properties of the High-Strength AlZnMgCuNiSi Alloys*, J. Mater. Res. 18 (3), 2003, pp. 635-641

[44] Barta Jr., C., Barta, C., Sestak, J.: *Thermophysical Research under Microgravity (Space Laboratory TITUS)*, Book: *”Intelligence in a Materials World“*, CRC Press, Boca Raton, Florida, USA

Aeroelastic Analysis and Experiment of an Airliner Half-Wing Model

Aeroelastická analýza a experiment modelu izolovaného polokřídla velkého dopravního letounu

Ing. Jiří Čečrdle, Ph.D., Ing. Jaromír Maleček, CSc / VZLÚ, Plc., Prague

The paper deals with aeroelastic analysis and experiments of the isolated half-wing of the research wind tunnel model EuRAM (European Research Aeroelastic Model) performed at VZLU in the frame of the projects *"Active Aeroelastic Aircraft Structures"* and *"Research on Strength of Low-weight Structures with Special Regard to Airplane Structures"*. The half-wing model is a part of the complete four jet engine airliner wind tunnel model.

The model stiffness and modal characteristics were analytically and experimentally verified. The main interest was focused on the evaluation of the model aeroelastic characteristics, especially flutter, static and dynamic effectiveness of unconventional control surfaces, and aeroelastic response to the dynamic loads. Analytical and experimental results were compared to verify and update the analytical models. The results were also used for efficient planning and organization of the more expensive experiments on the complete aircraft wind tunnel model.

Příspěvek pojednává o výpočtech a zkouškách aeroelastického modelu izolovaného polokřídla výzkumného demonstrátoru EuRAM (European Research Aeroelastic Model), které byly provedeny ve VZLÚ a.s. v rámci projektů *"Active Aeroelastic Aircraft Structures"* a *"Výzkum pevnosti hmotnostně úsporných konstrukcí, zejména letadlových"*. Model poloviny křídla je součástí modelu celého širokotrupého velkého dopravního letounu se čtyřmi proudovými motory.

Analyticky i experimentálně byly ověřeny tuhostní parametry a modální charakteristiky. Těžiště zájmu spočívalo ve vyšetření aeroelastických vlastností modelu, zejména flatru, aerodynamických charakteristik poddajného křídla, statické a dynamické účinnosti různých typů nestandardně umístěných řídících plošek a aeroelastických odezev na dynamická zatížení. Výsledky výpočtů a experimentů byly vzájemně porovnány za účelem verifikace, event. naladění výpočtových modelů. Výsledky dále posloužily pro účelné plánování a organizaci nákladných experimentů na modelu celého demonstrátoru v rozměrnějším aerodynamickém tunelu.

Keywords: Keywords: half-wing model, aeroelastics, flutter, stiffness, modal analysis, measurements.

1. Introduction

From 2002 to 2005 the VZLU Group of Aeroelasticity was involved in the project *"Active Aeroelastic structures (3AS)"* [1] of the 5th EC Framework Program. The project was focused on the research and development of new concepts for the aircraft structures improvements by exploiting their aeroelastic deformations [2], [3]. Planned achievements were to decrease the structure weight, the control surfaces area, the aerodynamic drag etc., and thus to operate aircraft more economically. Specific concepts were analytically and experimentally verified using several demonstrators [4]. One of them was the so-called EuRAM (European Research Aeroelastic Model). The EuRAM wind tunnel model represented a four-engine jet airliner; the model wing span was 5.2 m and its total mass 220 kg (Fig. 1). The concept *"Active Aeroelastic Wing Tip Control (AAWTC)"* was validated by means of the EuRAM wing component model. The main aim of the project task was to develop and verify the active control system by means of conventional and new unconventional aerodynamic control surfaces.

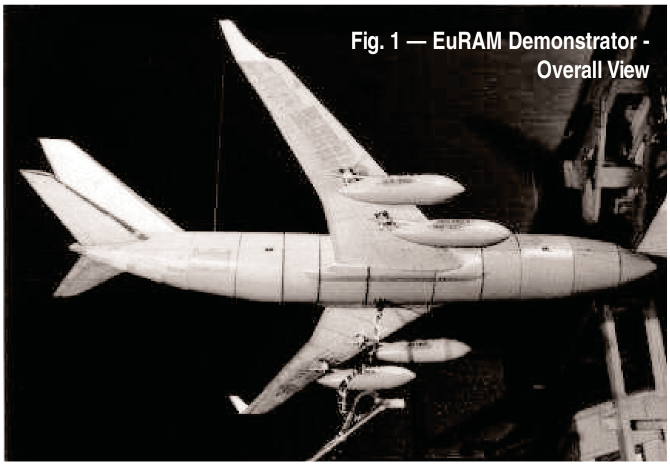
Fig. 1 — EuRAM Demonstrator - Overall View

Measurements of the isolated wing were performed at VZLU [5], [6]. To support the experiments various types of analyses were performed [7], [8], especially to clarify an unusual low level of the lift curves slopes obtained from experiments. On the one side, experimental results were used to verify and update analytical models. On the other side, analyses results were used to support the experiments.

Also, a database of experimental results for several wing configurations was used to develop and validate the analytical methods and procedures, especially calculation of the aeroelastic response due to kinematical excitation by a hydraulic cylinder and aerodynamic excitation by the deflection of the uncommon control surface; aileron placed in front of the wing tip chord (tip aileron -TA). Above-mentioned work was performed after the *3AS* project in frame of the project *"Research on Strength of Low-weight Structures with Special Regard to Airplane Structures"*.

2. Motivation

Main aim of the task was to conduct research on and verify the *Active Aeroelastic Wing Tip Control* concept on the half wing component of the EuRAM with the active control system off

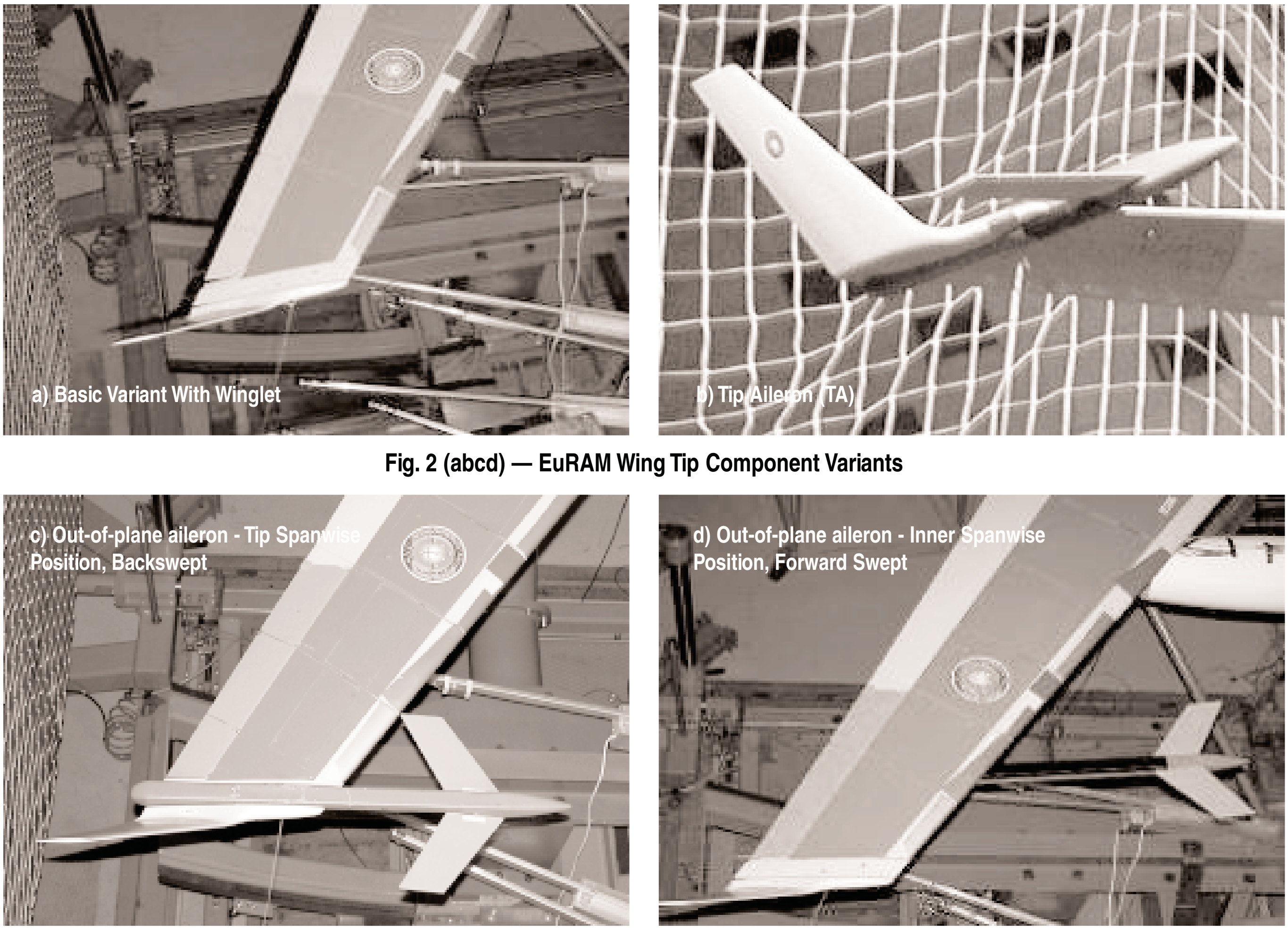

Fig. 2 (abcd) — EuRAM Wing Tip Component Variants

and on. During the initial analyses and wind tunnel tests flutter with a mode dominated by outer engine horizontal bending was detected. The wing tip control surfaces didn't turn out to be effective for suppression of such a flutter type. Therefore the initial test plan was modified. The active control device efficiency was checked out on the EuRAM complete model and the work on the half-wing component model was focused particularly on the investigation of static and dynamic aeroelastic characteristics.

3. Demonstrator description

3.1 Hardware model

The EuRAM wing component model was designed and manufactured by the Russian Research Institute TsAGI. Stiffness parameters were simulated by a duralumin beam. Wing segments were fixed to the wing beam. The engines were attached to the wing beam by short elastic beams. The wing was equipped with inboard (IA) and outboard (OA) ailerons, optionally with the tip aileron (TA) on the wing tip or with the out-of-plane aileron (OPA) (fig. 2). The TA and OPA could be attached with pylons of three different lengths. The pylons of the OPA could be placed on the wing tip and under the wing plane. The halves of the OPA and TA could be installed with forward or backward sweep angle. The ailerons were driven by miniature hydraulic cylinders through push-pull rods. The wing was equipped with a winglet by default.

3.2 Analytical model

Analyses were performed by means of the finite element methods using the MSC.NASTRAN program system. The model is idealized as a dynamic beam model; stiffness is modeled by mass-less beam elements placed on the elastic axis, the stiffness of engines mounts are modeled via spring elements. Mass characteristics are incorporated by means of concentrated mass

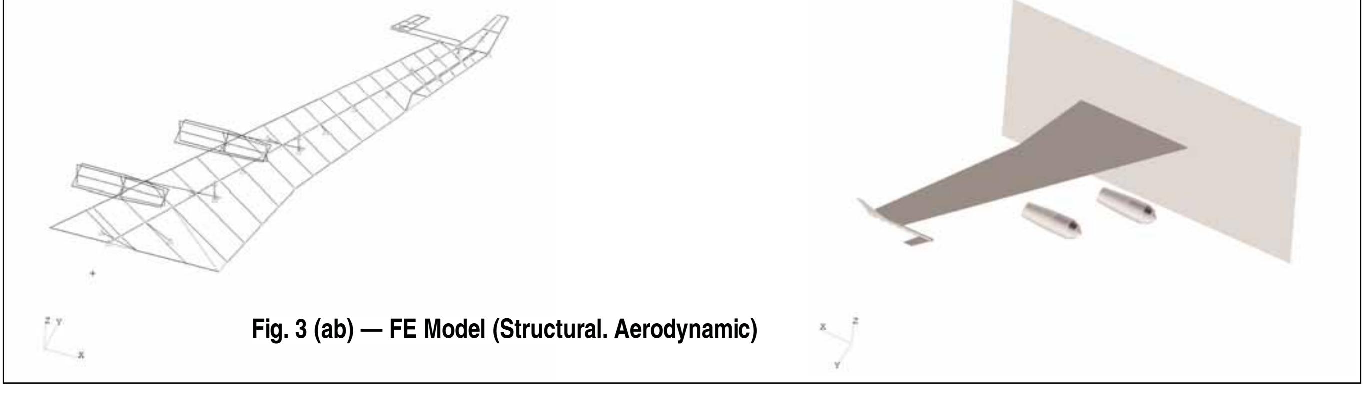

Fig. 3 (ab) — FE Model (Structural. Aerodynamic)

elements including appropriate moments of inertia. The model also includes various types of conditions for modeling specific relations, for visualization, and for connection with the aerodynamic model etc. The wing was cantilevered at the root, as implemented during the experiments. During the project, the model was updated and improved several times according to most recent information.

The aerodynamic model was created using the aerodynamic *Wing — Body Interference Theory*. Wing, winglet and splitter plate (to prevent the induced effects at the wing root part) were modeled by means of Doublet — Lattice panels, engines were modeled as Slender and Interference Bodies. Connections between structural and aerodynamic models were realized by means of beam splines. The structural and aerodynamic model (configuration with TA) is shown in Fig. 3.

4. Stiffness test

As a first step the mass and stiffness model parameters were verified. The wing was loaded by concentrated forces in vertical and horizontal direction and by a torsional moment. Deformations were scanned by incremental potentiometers. For example, a torsion moment was applied by a couple of weight forces on the wing tip (Fig. 4). The torsional unit deformation is presented in Fig. 5.

To verify the FE model stiffness characteristics a linear static calculation was performed. Applied loads were equal to the maximum loads applied during the stiffness tests [5], e.g. F_y = 25,898 N; F_x = 34,531 N; M_{EA} = 13,363 Nm. Considering the poor agreement of deformation curves (analysis and test), especially in torsion around the elastic axis, the FE model was tuned to experimental deformation curves using the material properties as global parameters (Fig. 6ab).

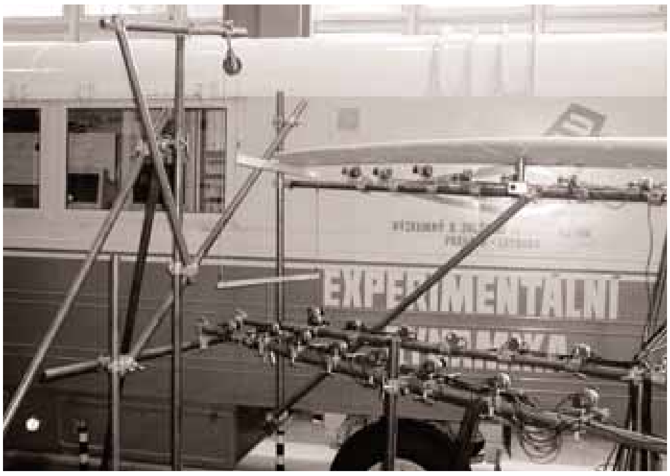

Fig. 4 — Stiffness Test - Torsional Load

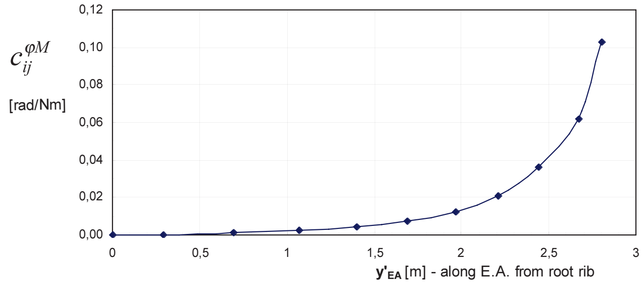

Fig. 5 — Torsional Flexibility Influence Coefficient

5. Ground vibration test

A modal analysis was performed to verify wing stiffness and mass characteristics by comparison of experimental and analytical results. Natural frequencies obtained by analysis by means of the Lanczos Method together with experimental ones obtained by the PRODERA system (Fig. 7) are presented in Tab. 1. It is worth mentioning that the experimental and analytical results were in satisfactory agreement. The GVT results (natural frequencies, generalized masses and damping and mode shapes) were used for verification and tuning of the FE model and for the flutter and dynamic response analysis.

Tab.1 — Modal Characteristics Summary

	EXPERIMENT		ANALYSIS	
mode shape title	#	f_{GVT} [Hz]	#	f_{FEA} [Hz]
1st wing vertical bending	1	1,629	1	1,723
1st inner engine horizontal vibrations	2	2,713	2	2,559
1st outer engine vertical vibrations	3	3,239	3	2,966
1st outer engine horizontal vibrations	4	3,372	4	3,292
1st inner engine vertical vibrations	5	4,212	5	4,029
1st wing horizontal bending	6	4,655	6	5,015
2nd wing vertical bending	7	5,365	7	5,872
2nd inner engine horizontal vibrations	8	8,430	10	8,968
2nd outer engine horizontal vibrations	9	8,482	9	8,808
3rd wing vertical bending	10	10,270	11	12,296
2nd wing horizontal bending	11	12,770	12	15,415
1st wing torsion	12	15,160	17	19,333
2nd inner engine vertical vibrations	13	16,190	14	17,064
2nd outer engine vertical vibrations	14	16,770	13	16,802

6. Aeroelastic wind tunnel tests

6.1 Test arrangement

The tests were performed in the VZLU low-speed wind tunnel. It is an atmospheric closed circuit type design with an open test

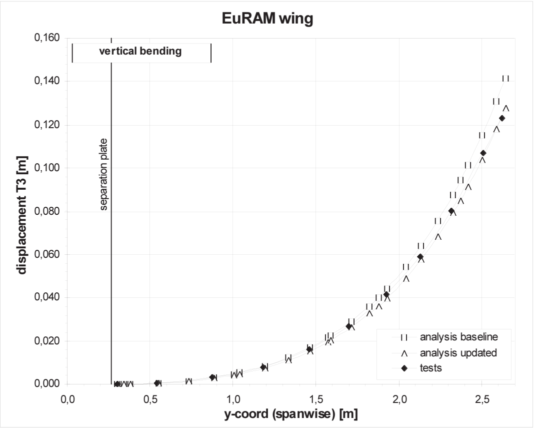

Fig. 6 (ab) — Linear Statics Analysis - Deformation Curves

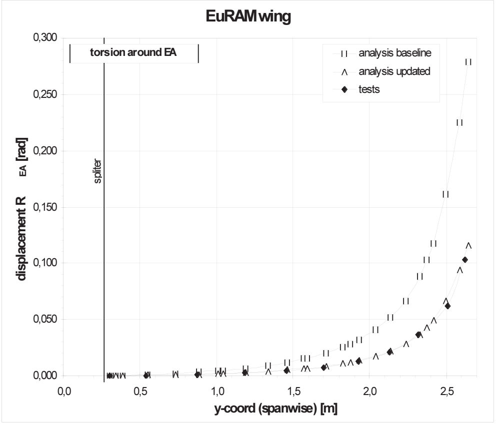

Fig. 7 — Ground Vibration Test

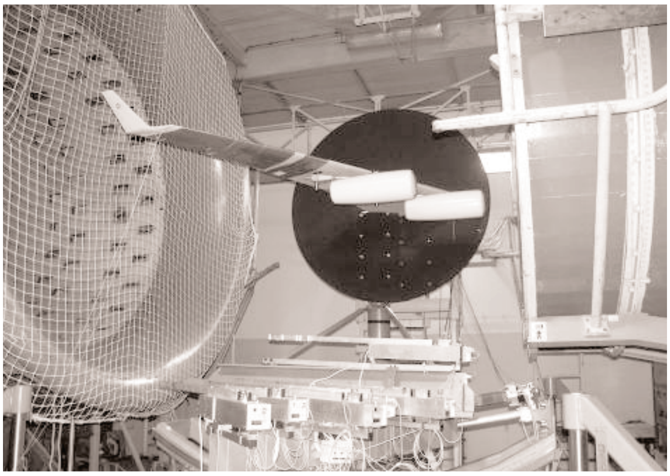

Fig. 8 — Wind Tunnel Static Test Arrangement

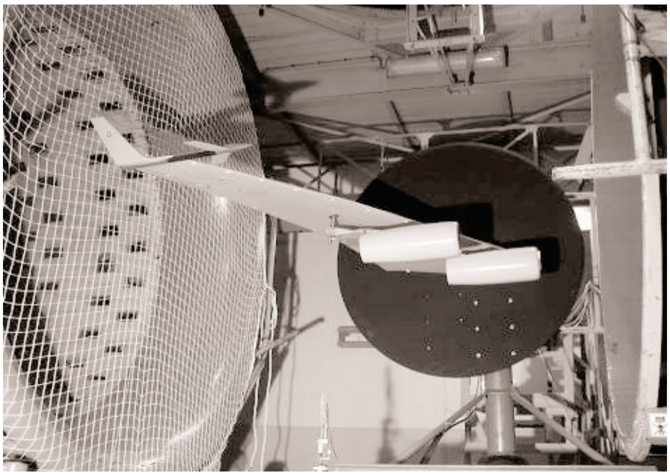

Fig. 9 — Wind Tunnel Dynamic Test Arrangement

section of 3 m diameter and 3 m length. The maximal flow speed is 70 m.s^{-1}.

The original aerodynamic strain-gauge balance and the existing manipulator for changing the angle of attack were used. Time and economic savings were realized by applying proven measurement procedures. The shortcoming of the relatively flexible balance was the introduction of elastic ”joint“ in the attachment stiffness scheme. However, the usage of an existing manipulator made it possible to employ the automatic angle of attack setting for static measurements at a given flow speed. Regarding results of the modal analysis, the original attachment was stiffed and designed in two arrangements: the first one for the static test with balance (Fig. 8) and the second one for the dynamic test with no balance (Fig. 9).

The static test was aimed at the measurement of the aerodynamic forces and moments using the aerodynamic balance, the internal model loads using strain gauges, and the model deformation. Aerodynamic forces and moments were scanned with the aerodynamic six-component strain-gauge balance (Fig. 10). Internal model loads were scanned by strain gauges at the wing root, half span and tip. The strain-gauge signals were calibrated to get the vertical and horizontal bending moments and the torsional moment. Deformations were scanned by inclinometers applied spanwise in three cross-sections of the wing beam at the elastic axes and at the outboard engine. Deformations were also scanned by an optical contactless measurement technique (four pairs of marks spanwise), which are based on the measuring the change of distance of the laser mark projected to the elastic model from the indicator. Model deformations were assessed from the mark picture in the TV signal shift (only in one direction). Finally the deformations of the wing tip were scanned by the photogrammetric method. The translation and torsion of the wing tip were identified from the trajectory of the marked points on the tip. The sampling frequency of the strain gauge signals, accelerometers and inclinometers was 200 Hz; the optical signal was scanned with a frequency of 8 Hz.

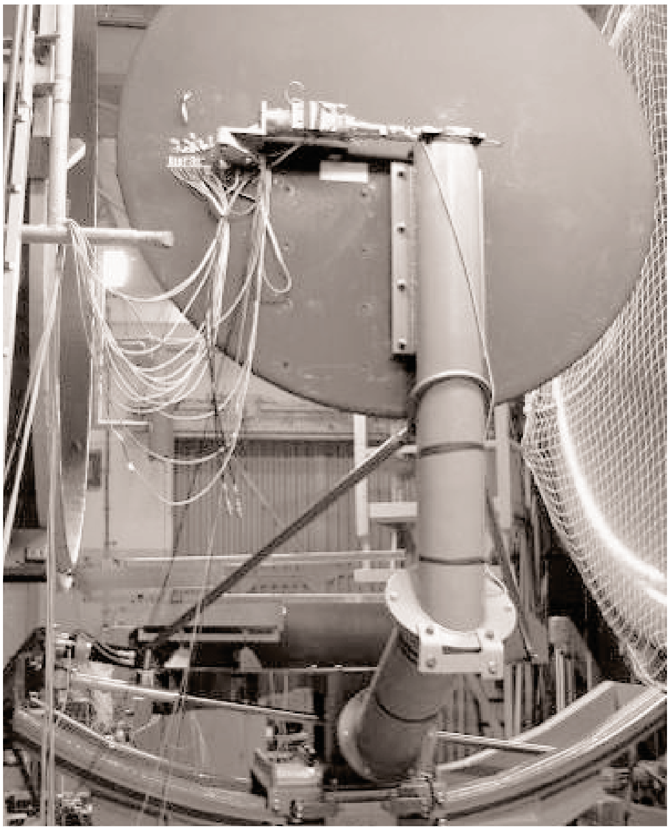

Fig. 10 — Strain-gauge Balance Arrangement

The kinematic excitation of the model for dynamic tests was generated by hydraulic cylinder acting at the outboard engine attachment. The maximum working displacement amplitude was 25 mm and the maximum force was 2500 N. The hydraulic pump supplied 21 MPa pressure for the kinematic excitation and 8 MPa for the actuation of the control surfaces.

The PC used for data acquisition and for excitation control was equipped with NI 6034 E and NI 6036 E acquisition cards.

Computer programs for data acquisition and conditioning and for exciter and aileron control were created by means of the LabVIEW system. For the optical contactless method computer programs were generated in the ”Control Panel“ system. The wind tunnel control and aerodynamic data scanning system used LabVIEW as well.

The static tests were divided into two phases. First, the angle of attack α and the aileron deflections δ were constant and the flow velocity was varied in the investigated range. Second, the flow velocity V and the aileron deflection δ were constant and the angle of attack α was varied in the investigated range.

In the dynamic tests for flutter stability investigation the model was excited by the air turbulence, by impulses applied with wires and by the exciter (frequency sweep). Frequency response functions of the model were measured by linear sweep excitation also by selected types of aileron imputs.

The following parameters could be varied: - the engine position (x, y), - the angle of attack (α), - the aileron deflection (δ) of the IA, OA, TA, OPA, - the chordwise position of the TA/OPA, - the spanwise position of the OPA, - the vertical position of the TA/OPA, - the sweep of the TA (backward, forward) and - the sweep of the OPA (backward, forward, back/forward).

6.2 Wind tunnel static test results

Dependencies of the lift coefficient c_L, roll moment coefficient m_x and pitch moment coefficient m_y on the angle α, flowspeed V and aileron deflection δ for various aileron parameters were measured. Graphs of the effectiveness in lift c_L^{α}, c_L^{δ}, in roll m_x^{α} , m_x^{δ} and in pitch m_y^{α} and m_y^{δ} were computed from measured aerodynamic coefficients. The comparison of effectiveness in lift c_L^{δ} of various ailerons is shown in Fig. 11. New types of ailerons (TA, OPA) are more suitable considering control reversal than conventional ones (OA, IA).

Data from strain gauge at the root of the wing beam were scanned and calibrated as the vertical bending moment M_{x1}, the horizontal bending moment M_{z1} and the torque moment M_T. The dependence of the vertical bending moment M_{x1} of the basic wing configuration on the flow speed V for fixed conventional ailerons at eight values of angle of attack α and at seven air speeds is shown in Fig. 12. The load envelope was used for the on-line monitoring of the model safety. Deformations of the wing tip measured by the photogrammetric method are presented in Fig. 13 at three angles of attack α. Translational deformations measured by the contactless optical method are presented in Fig. 14 (spanwise distribution and air speed variation).

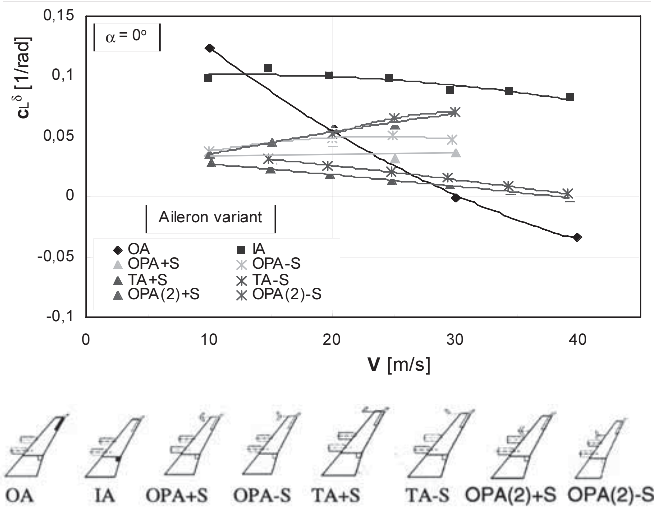

Fig. 11 — Aileron Effectiveness in Lift

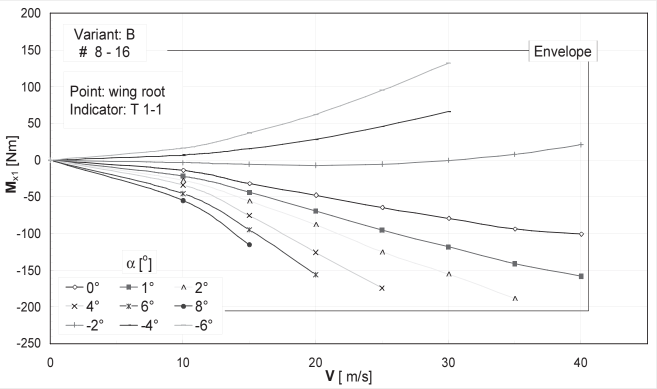

Fig. 12 — Loads - Bending Moment, Basic Variant Without Ailerons

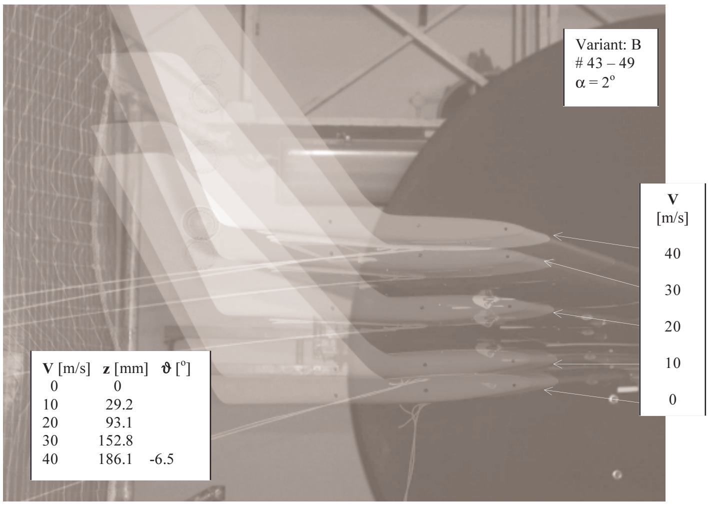

V [m/s]	z [mm]	ϑ [°]
0	0	
10	29.2	
20	93.1	
30	152.8	
40	186.1	-6.5

Fig. 13 — Deformation of the Wing Tip - Photogrammetry

6.3 Wind tunnel dynamic test results

The demonstrator was excited by a harmonic exciter input at the point of the outer engine attachment. Transfer functions at different speeds (waterfall diagrams) have been used to determine a critical flutter state. A waterfall diagram of transfer functions is presented in Fig. 15. The test was interrupted at the speed V = 25 $m.s^{-1}$ considering dangerous lateral vibration of the outboard engine. The waterfall diagram in Fig. 16 shows the response function of the bending moment at the root of the wing beam. This type of the test has been used to verify the control surfaces dynamic effectiveness.

The flutter was investigated in detail in the dynamic test on the basic model configuration. The critical flutter condition was defined by the parameters V_{FL} = 26.5 $m.s^{-1}$ and f_{FL} = 3.1 Hz. The dominant motion was lateral bending of the outboard engine.

7. Aeroelastic analyses

7.1 Static aeroelasticity

Static aeroelasticity analysis deals with the aerodynamic loads redistribution due to structural elasticity and with the deformations due to these aerodynamic loads. Incremental aerodyna-

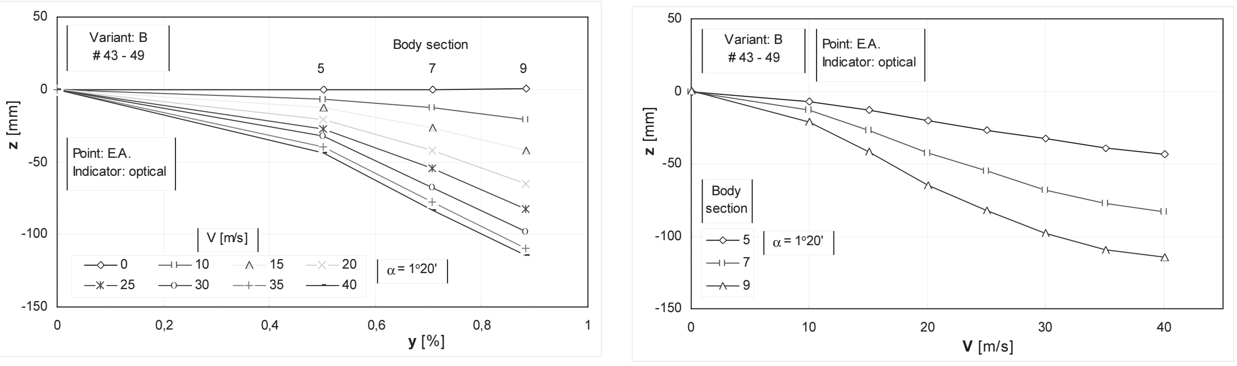

Fig. 14 — Deformation - Contactless Optical Method, Vertical Translation (Basic Variant - No Ailerons)

mic lift and moment values and their spanwise distribution are described by the slopes of the lift and moment curves. The experimental values are evaluated from aerodynamic forces and moments measured using the aerodynamic strain gauge balance. The lift curve slopes for different air velocities are presented in Fig. 17. The comparison of total aerodynamic forces was performed for the lift force, the pitching moment and the rolling moment. Agreement of the analysis and test results was found satisfactory for lift and rolling moment (differences up to 15%). Higher differences (roughly 50%) were found for the pitching moment. The probable reason is that the engine nacelles of the wind tunnel model are in fact annular wings and therefore generate more lift than simulated in analysis (see Fig. 3b). Considering the forward position of the nacelles, this lift causes a positive pitching moment.

The response of the flexible structure to aerodynamic loads was evaluated using influence functions. The example of the wing bending deformation is shown in Fig. 18ab. Agreement of results was found to be good, the differences are about 10 to 15 %.

7.2 Flutter

Flutter is a dynamic aeroelastic stability problem. The analysis was performed for the set of mode shapes presented in chapter 5 by means of the PK method of the flutter solution (1):

$$\left[M_{hh}p^2+\left(B_{hh}-\frac{1}{4}\rho\bar{c}V\frac{Q^I_{hh}}{k}\right)p+K_{hh}-\frac{1}{2}\rho V^2Q^R_{hh}\right]\{u_h\}=0 \quad (1)$$

Where: eigenvalue $p = \omega (\gamma \pm j)$; M_{hh}, B_{hh}, K_{hh} are modal mass, damping, and stiffness matrices; Q_{hh}^R, Q_{hh}^I are real and imaginary part of the aerodynamic matrix $Q_{hh}(M, k)$; $\gamma = g/2$ -decay rate coefficient; $\bar{c}$ - reference length; ρ - air density; V - air velocity; u_h - modal amplitude vector; M - Mach number; $k = \omega \bar{c}/2V$ - reduced frequency.

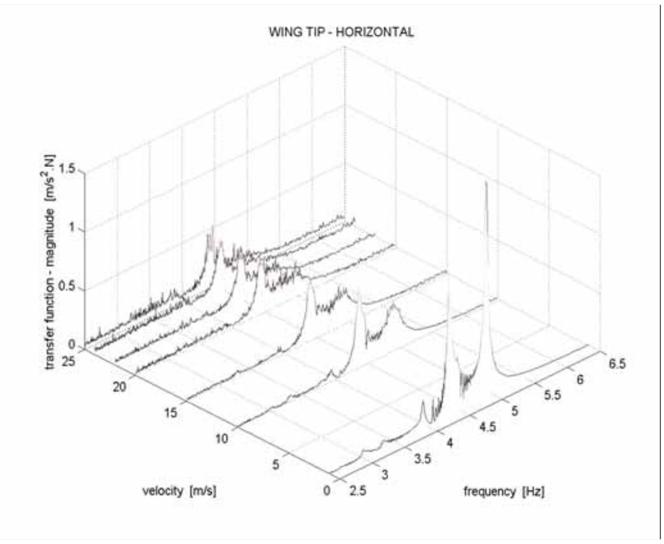

Fig. 15 — Transfer Functions, External Excitation, Frequency Sweep f = 2.5 ÷ 6.5 Hz

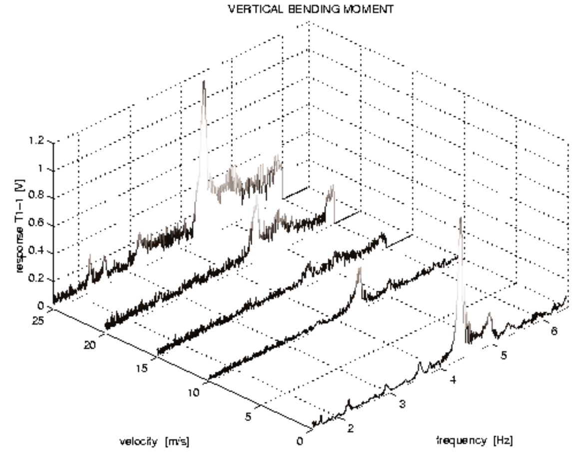

Fig. 16 — Transfer Functions, External Excitation, Frequency Sweep f = 2.5 ÷ 6.5 Hz

Two critical roots were found. A summary of the flutter critical speeds and frequencies for the nominal configuration (no TA) are shown in Tab. 2. The analytical value of the critical flutter speed with the 1st outer engine horizontal mode is roughly 4 m.s^{-1} lower, i.e. about 17 % than experimental value. The difference was caused by absence of structural damping in analysis. On the one hand, the damping ratios given by the ground vibration test were relatively low (the damping ratio for the 1st outer engine horizontal vibrations was $\alpha = 0.0015$), on the other hand the slope of the V-g curve is quite small and this fact increases the influence of the structural damping to the flutter speed. Therefore the agreement between analysis and test is satisfactory. Flutter instability for the 1st inner engine horizontal mode was not observed experimentally.

7.3 Aeroelastic frequency response analysis

Dynamic aeroelastic response analysis differs from flutter stability analysis in the presence of a right-hand side in the basic equations, which is non-zero and includes applied loads. Aeroelastic frequency response analysis is performed using modal coordinates and is based on equation (2):

$$\left[-M_{hh}\omega^2+jB_{hh}\omega+(1+jg)K_{hh}-\frac{1}{2}\rho V^2Q_{hh}(m,k)\right]\{u_h\}=\{P(\omega)\} \quad (2)$$

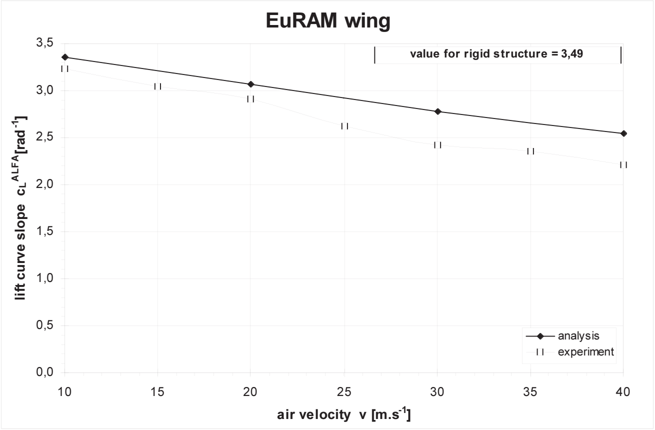

Fig. 17 — Lift Curve Slopes

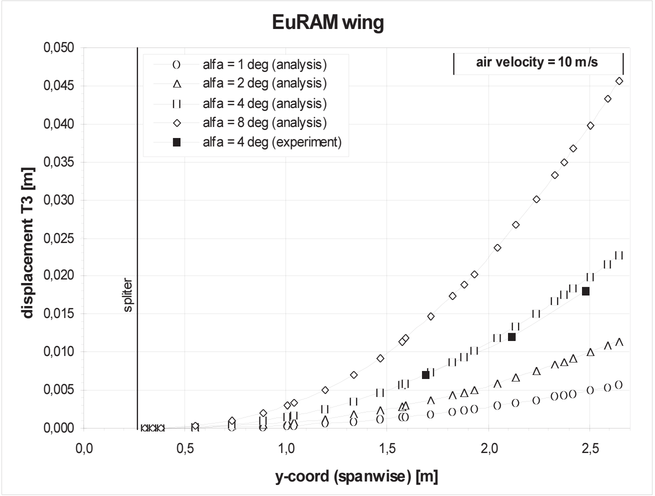

Fig. 18 (ab) — Wing Vertical Bending Deformations to the Aerodynamic Loads

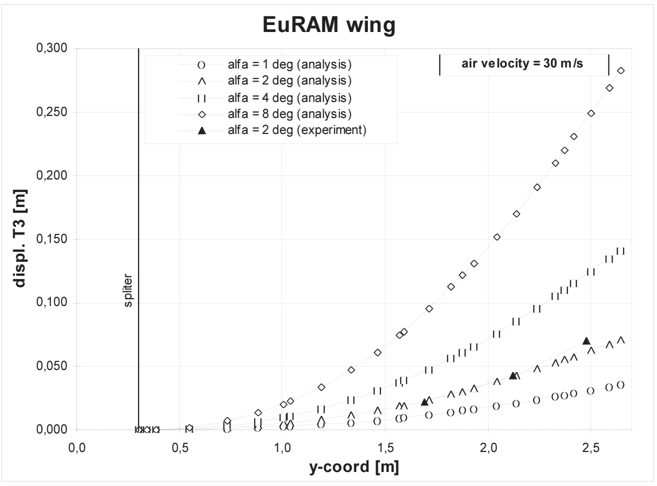

Tab. 2 — Flutter Results Summary

#	Mode shape title	V_{FL} [m.s^{-1}]	f_{FL} [Hz]
2	1st inner engine horizontal vibrations	28.4	2.6
4	1st outer engine horizontal vibrations	22.0	3.3

The left-hand side is identical to the K-method flutter equation (assuming harmonic motions); the right-hand side provides generalized aerodynamic or non-aerodynamic loading as a function of frequency.

Frequency response calculations were performed for the nominal configuration with the kinematic excitation and for the tip aileron configuration with aerodynamic excitation by control surface actuation.

7.3.1 Kinematic Excitation

As mentioned in the former chapter dealing with the experiments, kinematic excitation was implemented by means of a hydraulic cylinder attached through a rubber spring. The piston rod deflection (2 mm) and the spring constant (1480 N.m^{-1}) were chosen considering the structural response and the noise level. The excitation was carried out as a frequency sweep.

The installation of the excitation system produced changes in the wing normal mode characteristics and the structural damping, especially in the 1st wing-bending mode (frequency increase by +15%). However, the influence on the engine vibration modes was low.

Modeling of the excitation system is shown in Fig. 19. The direct method of enforced motion specification was used. Calculations were performed for several air speeds and an air density of $\rho = 1.225$ kg.m^{-3}.

A viscous model was used to describe the damping of the structure. The damping was introduced using values of damping ratio dependent on the frequency. The damping effect of the excitation system was described by the scalar damper placed in parallel with the excitation spring, the damping coefficient was tuned to match the amplitude of the 2nd wing vertical bending mode response. Considering the fact that damping was strongly influenced by the excitation system, the structural damping coefficients from modal tests could not be used. The damping coefficients for each mode shape were determined by tuning of the maximum response amplitudes to the experimental values for zero air velocity. The sensor showing the maximum amplitude in the relevant mode shape (wing tip, inner engine, outer engine, horizontal direction, vertical direction) was used for comparison with the relevant component of the related FE model grid point. Tuned damping coefficients were set using the frequencies of the related mode shapes. To compare analysis with experiments, signals from accelerometers placed at the wing tip in vertical and horizontal direction and placed at the front part of both engines were used. Comparison of results for the selected air speeds and degrees of freedom are presented in Fig. 20 a-d.

Fig. 19 — Kinematic Excitation

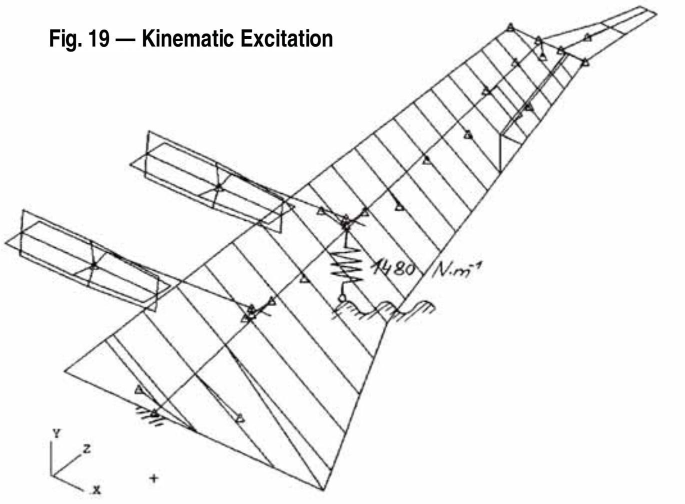

7.3.2 Aerodynamic Excitation

The aerodynamic excitation effect is based on the unsteady

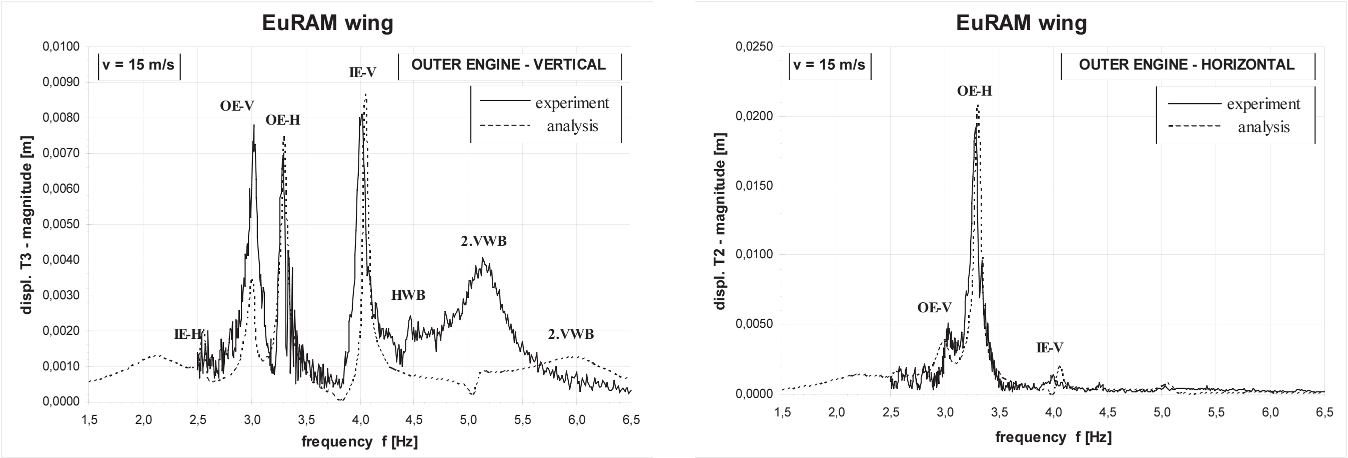

Fig. 20 (a-d) — Amplitude Characteristics - Comparison Analysis / Experiment

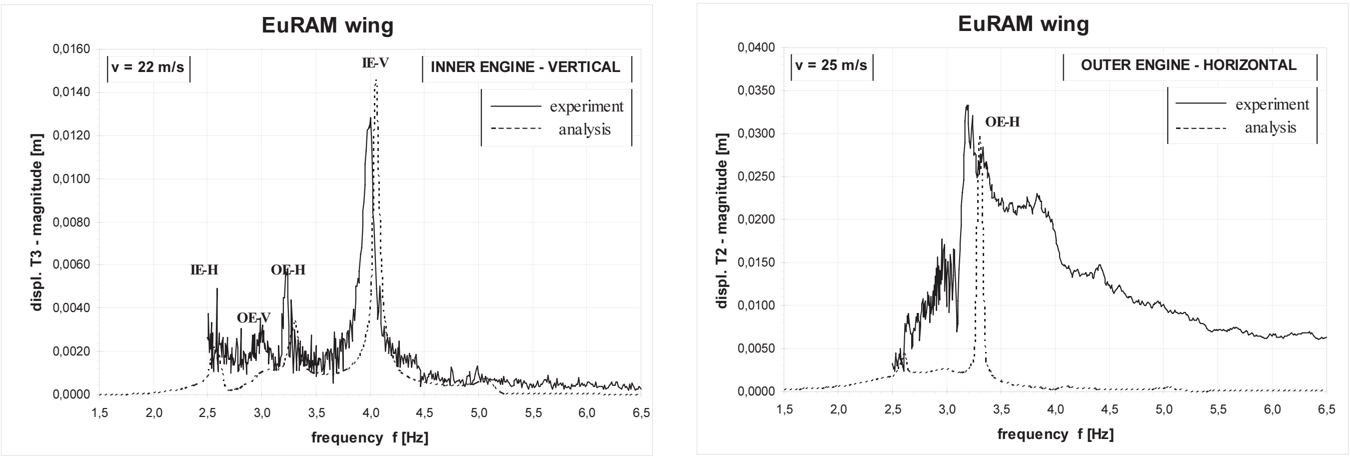

force or moment (lift, pitching moment), which is caused by an oscillation angle of attack at lifting surfaces. The excitation was generated by TA deflections, realized as a frequency sweep similar to the former example. Experimental deflection amplitudes were around 2.7 - 2.8 [degrees]. An exact setting of the deflection amplitude was not possible with the TA driving system. Calculations were performed for an air speed of 25 m.s^{-1}. The viscous structural damping was incorporated using the relative damping from modal tests, which were set as a function of frequency. Frequency values were taken from the flutter solution for appropriate air velocity. The TA deflection was specified at the TA root point by means of the Lagrange Multiplier Method. This method is adding extra degrees of freedom, which are used as force or moment variables to provide the appropriate enforced motion. For the enforced displacement, the equation of motion becomes:

$$[M_{dd}]\{\ddot{u}_d\}+[B_{dd}]\{\dot{u}_d\}+\begin{bmatrix}0 & I_{33} & 0\\ I_{33} & K_{33} & K_{3C}\\ 0 & K_{C3} & K_{CC}\end{bmatrix}\begin{Bmatrix}-q_3\\ u_3\\ u_C\end{Bmatrix}=\begin{Bmatrix}Y_3\\ P_3\\ P_C\end{Bmatrix} \quad (3)$$

Where: q_3 is the forces of constraint vector; u_3 is constraint displacements vector; Y_3 is vector of enforced displacement.

The value of the enforced displacement (TA angular deflection) was determined by the hydraulic piston rod translation, which was measured during experiments. The value of the TA angular deflection relatively to the airflow is set as a sum of the mentioned forced deflection and

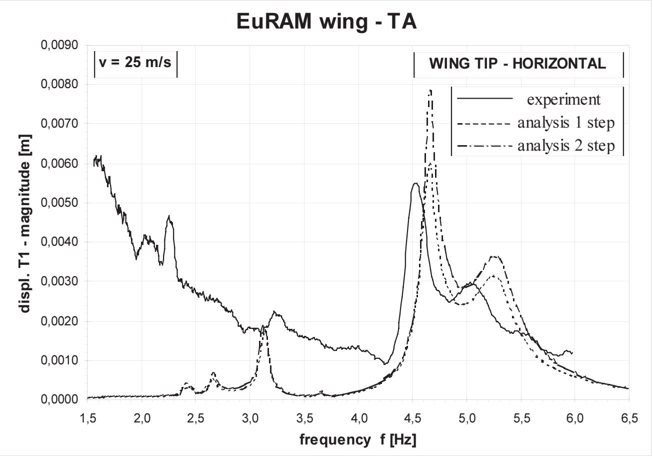

Fig. 21 (ab) — Amplitude Characteristics - Comparison Analysis / Experiment

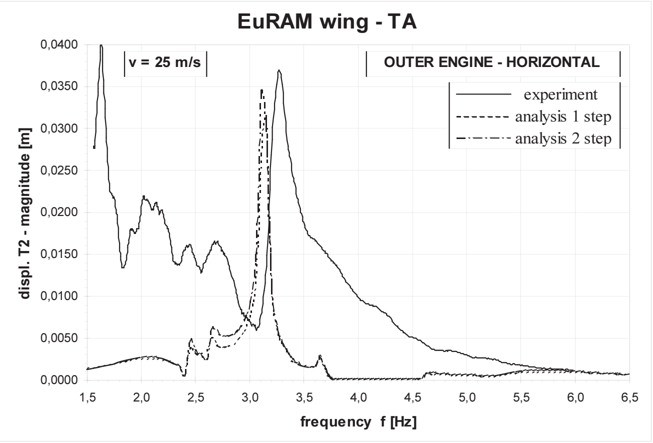

deformation of the structure (TA pylon). The latter component may be particularly significant if the deformation of the structure has torsional character. Calculations were performed in two steps. In the first step the TA deflection relative to the undeformed shape (determined by the piston rod translation) was set. Then the response to this excitation (real and imaginary part) at the TA root point (TA pylon) was added to the initial values. The calculation of the second step provided a response to the excitation signal, which included a structural deformation from the previous step. After that it was possible to stop the calculation process, since the changes of the structure response after the next step were barely noticeable.

The example results are presented as amplitude characteristics in the Fig. 21ab. Several important grid points of the structure were observed (especially the test pickups points). The comparison was performed for the step 1 (excitation set relatively to the undeformed shape) and step 2 (excitation set relatively to the deformed shape).

The agreement of experimental and analytical results was found to be acceptable. The main reason for discrepancies was the already mentioned fact, that the wind tunnel model engine nacelles were annular wings, but the analytical model considered nacelles as solid slender bodies with elliptic cross-section. Modeling of the annular rings would be possible for example by means of the ZAERO aeroelastic software package. Test calculations showed, that the flutter speed caused by outer engine lateral vibrations is quite dependent on the nacelle aerodynamic model. Also the poor quality of the excitation signal (harmonic waveform) due to friction in the TA driving system should be taken in account.

Blocking of the flow through the engine nacelles was tested during static wind tunnel experiments. Values of the c_L^α of the through-flow nacelles was roughly 15% higher than those with blocked flow.

8. Conclusion

An overview has been given on aeroelastic computations simulations and experiments with a wing component of a wind tunnel model of an airliner.

Calculations, especially dynamic response analyses were performed by means of the MSC.NASTRAN software. Procedures of incorporation of an aerodynamic excitation by the control surface deflections were implemented and tested.

Selected variants of the EuRAM starboard wing aeroelastic model with and without conventional and unconventional ailerons were tested in the VZLU wind tunnel. The aerodynamic characteristics, model structural loads and deformations were measured during the static wind tunnel test. The on-line monitoring of the load envelope was used for the model safety during the wind tunnel runs. Model structural deformations were measured by three independent methods: photogrammetric, optical contactless and using inclinometers.

The dynamic tests of the wing model determined the flutter stability of selected model variants. Frequency response functions were measured with kinematic excitation and with excitation by control surfaces.

The results of the wind tunnel test have been used mainly to validate the analytical model and to plan an efficient test of the complete aircraft model. Analyses results were compared with results of experiments. The agreement is good in most cases. The causes of discrepancies were detected and possibilities to improve the analysis model were indicated.

9. Acknowledgement

The paper deals with the VZLU participation in the 5th FP EC Project *”Active Aeroelastic Aircraft Structures“*, which was funded under contract of the European Union in the sphere of the EuRAM demonstrator relating activities. It is incorporated in the *3AS* project data-base.

Further work, mainly frequency response analyses and preparation of the publication were performed in the frame of the project *”Research on Strength of Low-weight Structures with Special Regard to Airplane Structures“* funded by the Czech Ministry of Education, project number MSM 0001066903.

10. References:

[1] Schweiger, J. - Simpson, J. - Suleman, A. - Cooper, J.: *Review of the European Research Project ”Active Aeroelastic Aircraft Structures“*, IFASD 05 (International Forum on Aeroelasticity and Structural Dynamics, International Conference, 28.6.-1.7.2005, Munich, Germany, IF-096, CD-ROM, ISBN 3-932182-43-X

[2] Kuzmina, S.I. - Schweiger, J. - Cooper, J. - Ampridikis, H. - Sensburg, O.: *Review and Outlook on Active and Passive Aeroelastic Design Concepts of Future Aircraft*, ICAS 2002 Congress, 2002, Toronto, Canada, ICAS-2002-432

[3] Moulin, B. - Karpel, M.: *Gust Loads Alleviation Using Special Control Surfaces*; Israel Conference of Aerospace Sciences, February 2005, Tel-Aviv - Haifa, Israel

[4] Schweiger, J. - Suleman, A. - Kuzmina, S.I. - Chedrik, V.V.: *MDO Concepts for an European Research Project on Active Aeroelastic Aircraft*; 9th AIAA/ISSMO Symposium on Multidisciplinary Analysis and Optimization, 4.-6.9.2002, Atlanta, Georgia, AIAA 2002-5403

[5] Maleček, J. - Čečrdle, J. - Chedrik, V.V. - Naiko, Yu.A.: *Analysis and Experimental Validation of an Aeroelastic Half Wing Model*; EUCASS 05 (European Conference for Aerospace Sciences), International Conference, 4.-7.7.2005, Moscow, Russia, 4.SP.08, CD-ROM

[6] Maleček, J.: *Experiments on the Airliner Aeroelastic Half-wing Model*; 4th Conference Dynamics of the Stiff and Flexible Bodies, 20.-21.9.2006, Ústí nad Labem, Czech republic, pp. 139-146, ISBN 80-7044-782-6

[7] Čečrdle, J.: *Aeroelastic Analysis of the EuRAM Demonstrator Isolated Wing by Means of the MSC.NASTRAN Program System*; MSC.Software Users Meeting 2004, Paper No. 15, Brno 26.-27.5.2004, CD-ROM

[8] Čečrdle, J.: *Analysis of the Airliner Half-wing Aeroelastic Model*; 4th Conference Dynamics of the Stiff and Flexible Bodies, 20.-21.9.2006, Ústí nad Labem, Czech republic, pp. 17-24, ISBN 80-7044-782-6

PVD Coatings as a Cadmium Replacement — Part I

Náhrada kadmia PVD povlaky — Část I

Ing. Martina Pazderová / VZLÚ, Plc., Prague; J. Macák, E. Machníková / Institute of Chemical Technology Prague, Department of Power Engineering

With increasing concern about toxic wastes produced by conventional sur-face treatment, there is a strong tendency to find some ecologically and economi-cally convenient resolution. PVD (physical vapour deposition) coatings are finding its utilization in most industries. In this paper, PVD coatings deposition processes, post-treatment possibilities, and evaluation methods are discussed. PVD coatings were subjected to corrosion salt spraying tests and coatings porosity, which repre-sents the main corrosion problem, was evaluated by electrochemical impedance spectroscopy (EIS). Some additional measurements were performed by SEM, EDAX, and AFM. The results obtained were confronted with cadmium corrosion and mechanical properties.

Rostoucí zájem o množství nebezpečných odpadů vznikajících při klasických povrchových úpravách vede ke snaze nalézt ekologicky a ekonomicky vhodnou náhradu. V celé řadě průmyslových odvětví našly své uplatnění PVD (fyzikální va-kuové napařování) povlaky. Článek se zabývá metodami nanášení PVD povlaků, možnostmi následné pasivace povrchu a vyhodnocovacími metodami. PVD povla-ky byly podrobeny korozní zkoušce v solné mlze a elektrochemická impedanční spektroskopie (EIS) byla využita pro stanovení poréznosti povlaku, neboť ta před-stavuje hlavní problém z hlediska koroze. Doplňující měření byla provedena meto-dami SEM, EDAX a AFM.

Keywords: cadmium, electrochemical impedance spectroscopy, physical vapour deposition.

1. Introduction

Using cadmium in metal plating and other applications results in significant emissions of cadmium in the environment. In the last decades, there has been a great effort to reduce the amount of toxic wastes generated from plating and us-age of plated components. Cadmium usage is restricted by Regulation No. 301/1998 [1] but some exceptions are specified there. Electroplated cadmium can still be used in marine, aerospace and military applications to coat fasteners, electronic components, springs, aircraft landing gear, components requiring high safety standards, and others. It enhances mechanical and physical properties of sub-strate materials due to its good conductivity, solubility, self-lubricating properties. In addition, electroplated cadmium has an unequalled corrosion resistance in ag-gressive environment [2].

As environmentally and technically clean alternatives to cadmium plating PVD and CVD coatings are often considered. During the last decades, CVD (chemical vapour deposition) and increasingly PVD (physical vapour deposition) coatings are finding its utilization in metal finishing. Vapour deposition methods are based on growth of the coating by condensation of selected gaseous solid on the surface of coated object. CVD technology compared to PVD, has fewer advan-tages and cannot be used for all materials. PVD coatings are used as functional, protective, or decorative coatings, respectively. Nitrides and carbides, mainly based on titanium, chromium, zirconium, and aluminium have gained attention due to their excellent properties: high hardness, chemical inertness, wear, and corro-sion resistance, respectively. Certain problem of PVD coatings application is cor-rosion resistance of the whole system coating-substrate. The growth of protective coating is closely connected to creation of pores and pinholes that may cause cor-rosion of the substrate (which is mostly less noble than coating).

Electrochemical impedance spectroscopy is still finding more utilization at monitoring of corrosion processes and their mechanisms [3-9]. EIS and adequate physical model of electrochemical reaction assist in finding information about elec-trode reaction, pore resistance, coating and substrate polarisation resistance, and dielectric layer capacitance at electrolyte/substrate interface. The results can be used for determination of coatings porosity and corrosion resistance [10-15].

2. Vapour deposition methods

2.1. *CVD*

Chemical vapour deposition (CVD) produces layers from gas phase with thickness of 0.1 - 10 μm, by means of chemical reaction. Working pressure can vary: approx. 1 - 50 hPa for low-pressure CVD (LPCVD), 50 - 100 hPa for medium-pressure CVD, and atmospheric pressure for atmospheric CVD (ACVD). CVD is an open system with a gas inlet and outlet and the equipment has follow-ing main parts: a gasification system, chemical reactor, which contains the samples to be coated, and an exhaust system for the reacted gas. Input compounds can be inorganic (e.g. halides, hydrides, carbonyls) or organic (alkyls, alkoxides, organometallics). CVD can be used for deposition of a large variety of compounds, provided the material can be dissolved in the gas phase.

The structure of the coating is the result of several steps: adsorption — de-sorption processes, surface reactions, surface diffusion, nucleation, layer formation, and aging processes in the layer during deposition. According to the method of chemical reaction activation CVD technology can be divided to thermal CVD (using heating of the reactor or the samples; laser irradiation) and plasma CVD. The later method was developed to decrease the deposition temperature. The respective processes are called plasma-activated deposition processes (PACVD) or plasma-enhanced CVD (PECVD).

High coating temperature limits the usage of CVD technology and is main reason of PVD predominance.

2.2. *PVD*

It's important to say that the coating's adhesion and number of pinholes, pores, and defects is dramatically influenced by the deposition method used. Generally, PVD deposition methods may be distinguished into two general catego-ries — sputtering and evaporation. The application of PVD coatings ranges from decorative to high-temperature superconducting films. Thickness of layers ranges from 10^{-10} to 10^{-3} m. A very large number of inorganic materials (metals, alloys, mixtures, etc.) as well as organic materials can be deposited by PVD technology. A hybrid PVD process is "ion plating", i.e. atomic film deposition process, in which the substrate surface and/or deposited film is subjected to a flux of high-energy particles, sufficient to cause changes at substrate/film interface. These changes may consist in film's adhesion, morphology, density, or stress [16].

Sputtering is a transfer from an indirect energetic projectile, as an ion, to a solid or liquid target, resulting in ejection of surface atoms or molecules. Target and substrate are placed in vacuum chamber evacuated to a pressure of 10^{-2} - 10^{-5} Pa. Target (cathode) is connected to a negative voltage supply and the substrate generally faces the target. Glow discharge is initiated after an inert gas (usually argon) is introduced into the evacuated chamber. Working pressure usually ranges 2.5 - 20 Pa.

Planar diode glow discharge sputter deposition is the simplest sputtering system, consisting of the cathode (target) and anode facing each other. Substrate is placed on anode. Target, usually water cooled, has two functions — source of coating material and electrode sustaining glow discharge. The distance between elec-trodes is usually 5 - 10 cm. Deposition rate is mainly determined by the power density at the target surface, by the size of the sputtered area, by source — substrate distance, working pressure, and source material. Sputtering is widely used owing to its simplicity but has several disadvantages: low deposition rate, sub-strate heating caused by the high-energy particles bombardment, and relatively small deposition area.

By applying magnetic field to the sputtering system magnetron sputtering was developed, which has greatly increased ionization efficiency. There are several configurations of magnetron sputter deposition setup. Magnetron can be cylindrical, planar, and in the form of S-gun. Cylindrical magnetron is very useful to prepare uniform coatings over large areas, because it employs long cathodes. Furthermore, this method is effective for coating of complex-shaped objects. Planar magnetron is used for preparation of metallic and dielectric films, using higher deposition rates. To deposit films on thermally sensitive substrates (e.g. electronic devices) S-gun magnetron can be used, because this method allows good isolation of the substrate from the plasma. Magnetron also can be balanced and unbalanced. The later is preferable one because the plasma may access the substrate easily and the deposition process is more efficient.

In the evaporation process, vapors are produced from source which is heated by various methods. The system consists of an electron-beam-heated evaporation source to vaporize the desired material. The possible heat sources are resistance, induction, cathodic and anodic arc, electron beam, or laser. Evaporation is carried out in a vacuum of 10^{-3} - 10^{-8} Pa. An often met problem is droplet ejection from the target during the deposition causing coatings worth quality. It can be solved by use of a filtered arc where the ion stream is extracted by an electromagnetic field and the ions are condensed to deposit a film.

Great PVD process adaptability enables deposition of variety of materials, i.e. metals, alloys, semiconductors, superconductors, and polymers and preparation of different composite types (particulate, fibrous, and laminate). Each process has some advantages and some disadvantages, which should be considered in terms of following usage of coated subject. Fig. 1 shows some examples of PVD processes.

3. Polymers

Conducting polymers have been the topic of a large number of investigations during the last decades. Their unique properties such as mechanical strength, electrical conductivity, corrosion stability, and possibility of both chemical and electrochemical synthesis make them useful in wide area of applications: rechargeable batteries, electrochromic displays, electrochemical sensors and capacitors, and in the last few years in active corrosion protection. Unfortunately, thin films of conducting polymers can provide protection for a relatively short period. Therefore, it will be necessary to combine advantages of conducting polymers and classical coatings to obtain better corrosion protection of common metals, especially mild steel. Aging process decreases the conductivity that is important information for practical application. Basic conductive polymers are e.g. polyacetylene, polyethylene, polyfurane, polypyrrole, polythiophene, polybenzene, or polyaniline, and their derivates [17].

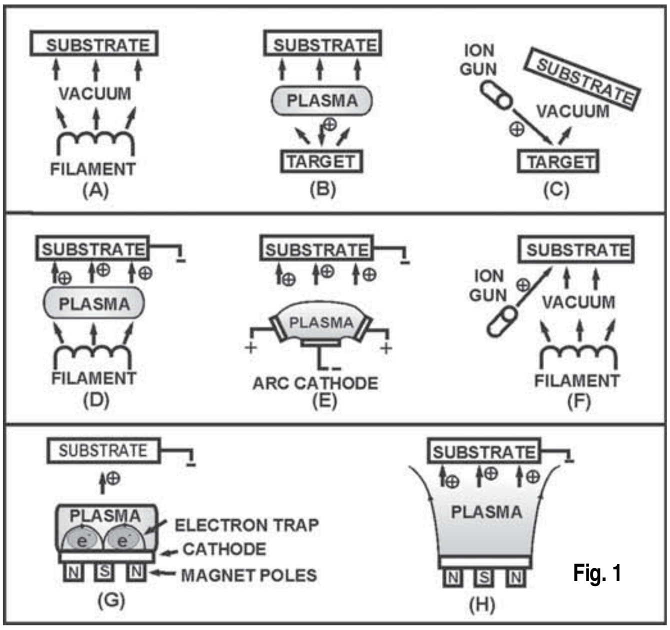

Fig. 1 — scheme of some PVD processes (A) evaporation, (B) plasma sputtering, (C) vacuum sputtering, (D) thermal ion plating, (E) arc-beam ion plating, (F) Ion Beam Assisted Deposition, (G) balanced magnetron sputtering, (H) unbalanced magnetron sputtering

All the mentioned polymers prove unique physical and chemical properties, very good chemical and thermal stability in oxidizing, easy synthesis, non-toxicity, good electrical and optical properties, and relatively low price. These polymers en-hance the substrate corrosion resistance due to formation of homogenous and adhesive films of a thickness in nm - μm.

3.1. *Polymerisation processes*

Polymerization proceeds by two general processes — chemical and electro-chemical. To gain a good coating by monomers polymerization it is necessary to link enough molecules and use appropriate catalyst of polymerization.

Chemical polymerization is an easy method for polymers synthesis due to monomers primary oxidation from aqueous and organic environment using very strong oxidizer (e.g. $K_2Cr_2O_7$, $KMnO_7$, $Ce(SO_4)_2$, $Cu(ClO_4)_2$, N-methylpyrolidone, $(NH_4)_2S_2O_8$, $FeCl_3$, $Fe(ClO_4)_3$). During oxidation an active cation radical are generated which interact with another monomer's molecule forming oligomer or insoluble polymer. Final product of volume polymerization is insoluble powder solid. Polymer quality depends on reaction conditions — solution concentration, oxidizer/monomer ratio, reaction temperature, surface treatment of coated material. Disadvantage of chemical polymerization is impossibility to reduce or stop the reaction. Chemical polymerization can be used for film preparation on the substrate surface by spontaneous formation of film from polymerization solution or by surface enrichment with monomer or oxidizer (ion exchange mechanism or deposition of insoluble layer). These films have good adhesion and consequent conductivity is higher than that of electrochemically formed films. Hydrophilic and hydrophobic surface, insulator and conductive substrate (e.g. metal, glass, ceramics, textile, polymer, etc.) can be coated by chemical polymerization.

Electrochemical polymerization is very effective in preparation of conductive polymers. Polymeric film can be deposited directly on the substrate. Electrochemical deposition is possible only with conductive materials, impossible with insulates. Surface morphology, porosity, and reductive activity of polymeric layers depend significantly on synthesis conditions — type of method, potential, current density, monomer type, electrolyte, its concentration and pH, etc. Poor adhesion can be enhanced by surface pre-treatment, e.g. passivation. Three different electrochemical methods are used for conductive polymers synthesis — cyclic voltammetry, potentiostatic method, and galvanostatic method. The last mentioned is the most significant method for conductive polymers electrochemical deposition. Electro-chemical polymerization can be carried out in organic and aqueous solutions, both acid and neutral and sometimes even basic environment. Polymerization rate de-pends on monomers and oxidizers concentration. High oxidation potential of monomer may be problematic (e.g. pyrrole +0.7 V vs. SCE, thiophene +1.6 V vs. SCE, aniline range -0.2 and +1.2 V vs. SCE, benzene +2.0 V vs. SCE). Technical metals dissolve at much lower potentials (e.g. Zn -1.0 V vs. SCE, Fe -0.68 V vs. SCE, Al -1.9 V vs. SCE) therefore the working electrode dissolves preferentially instead of monomers oxidation. Consequently metal dissolution rate must be reduced by appropriate solvent, supporting agents, or suitable surface pre-treatment of working electrode.

3.2. *Polyaniline*

Among the large number of electroconducting polymers, polypyrrole and polyaniline (PANI) are the most promising ones for corrosion protection. Neverthe-less, lower price of aniline monomer comparing to pyrrole makes PANI more chal-lengeable. Polyaniline is probably the oldest known synthetic polymer. The main problem related to the electrochemical polymerization of PANI on mild steel is dis-solution of bare metal in the beginning of polymerization, during so-called induction period, due to the high polymerization potentials of +0.4 up to 1.0 V, so only few types of electrolyte suitable for PANI deposition on mild steel were reported.

3.3. *Polypyrrole*

As mentioned above polypyrrole (PPY) is one of the most promising conducting polymers for corrosion protection. PPY has linear structure connected through α and α^1 positions in pyrrole nucleus. It is chemically stable, creates homogenous and adherent layers, and its electropolymerization is relatively easy and prompt in standard conditions.

4. Electrochemical impedance spectroscopy

Impedance spectroscopy (EIS) has been shown to be a powerful technique for the characterization of electrochemical systems. However, like any other electrochemical technique, EIS does not provide a direct measure of the governing physical phenomena. Interpretation of impedance data requires identification of appropriate models and this ambiguity inherent in interpretation of impedance spectra can make the evaluation difficult. Despite these problems, in recent years, impedance spectroscopy has found widespread application for characterization of materials. It is routinely used in the characterization of coatings, batteries, fuel cells, and corrosion phenomena.

The fundamental approach of all impedance methods is to apply a small amplitude sinusoidal excitation signal (voltage or current) to the system under investigation and to measure the response (current or voltage). The usual approach in interpreting impedance spectra is to regress a model to the data. The models employed are typically linear and assume conditions of a sinusoidal steady state. It is important, therefore, that the impedance response be characteristic of a system that is causal, linear, and stable. The conditions of linearity can be achieved by using sufficiently small amplitude perturbations. The condition of stability requires that the system returns to its original conditions when the perturbing signal is terminated.

The electrochemical cell in an EIS experiment can consist of two, three, or four electrodes. The three-electrode configuration is the most common for typical electrochemical applications. Usually the electrode under investigation is called the working electrode, the electrode necessary to close the electrical circuit is called the counter electrode, and the third electrode (reference) is used to determine or control the potential of the working electrode precisely. Since the absolute potential of a single electrode cannot be measured, all potential measurements in an electrochemical systems are performed with respect to a reference electrode. A reference electrode, therefore, should be reversible, and its potential should remain constant during the course of the measurement.

Impedance data can be represented in Nyquist (real part of impedance against the imaginary part) or Bode (modulus of impedance and the phase shift are plotted as a function of frequency) diagrams. The advantage of Nyquist representation is that it gives a quick overview of the data and one can make some qualitative interpretations. Modulus of impedance and the phase shifts are plotted as a function of frequency in two different diagrams. Bode plots can be advantageous in presentation of high frequency-low impedance phenomena.

5. Conclusions

In this study, PVD coatings were submitted to the salt spraying test, electro-chemical measurement, and mechanical tests to find complex corrosion protection characteristics. EIS was used for investigating the corrosion performance of PVD coating/steel systems without significant interfering to the ongoing corrosion processes. Relevant equivalent circuits were suggested with the aim to identify different stages of the corrosion behaviour of the given coatings.

6. References:

[1] *Vyhláška č. 301/1998 Sb.* (Notice No-301/1998 Coll.)

[2] *Final Report J316/Cadmium*, (2001)

[3] C. Liu, A. Leyland, S. Lyon, A. Matthews: *Surf. Coat. Technol.* 76-77 (1995) 615-622

[4] M. Tomlinson, S. B. Lyon, P. Hovsepian, W-D. Munz, *Vakuum 53* (1999) 117-121

[5] M. Ürgen, A. F. Çakir, O. L. Eryilmaz, C. Mitterer: *Surface and Coatings Technology* 71 (1995) 60-66

[6] S. H. Ahn, Y. S. Choi, J. G. Kim, J. G. Han: *Surf. Coat. Technol.* 150 (2002) 319-326

[7] I. Milošev, H.-H. Strehblow, B. Navinšek: *Thin Solid Films* 303 (1997) 246-254

[8] D. K. Merl, Panjan, M. Čekada, M.Maček: *Electrochemica Acta* 49 (2004) 1527-1533

[9] C. Liu, Q. Bi, A. Matthews: *Corrosion Science* 43 (2001) 1953-1961

[10] C. Robyr, P. Agarwal, P. Mettraux, D. Landolt: *Thin Solid Films* 310 (1997) 87-93

[11] C. Liu, Q. Bi, A. Leyland, A. Matthews: *Corrosion Science* 45 (2003) 1243-1256

[12] C. Liu, Q. Bi, A. Leyland, A. Matthews: *Corrosion Science* 45 (2003) 1257-1273

[13] C. Liu, A. Leyland, S. Lyon, A. Matthews: *Surf. Coat. Technol.* 76-77 (1995) 623-631

[14] L. F. Senna, C. A. Achete, T. Hirsch, F. L. Freire Jr.: *Surf. Coat. Technol.* 94-95 (1997) 390-397

[15] S. H. Ahn, J. H. Lee, H. G. Kim, J. G. Kim: *Appl. Surf. Science* xxx (2004) xxx-xxx

[16] P. J. Martin, D. R. Mckenzie: *Application of vacuum arc science and technology*, Handbook of vacuum arc science and technology

[17] E. Machníková: *Protikorozní elektrochemicky syntetizované povlaky*, (2005)

Harmful Gas Dispersion around the Train Station

Disperze škodlivých plynů kolem nádraží

Mgr. Radek Ulman, RNDr. Jiří Drbohlav, D. Zachoval / VZLÚ, Plc., Prague,
Z. Jaňour / Institute of Thermomechanics, Czech Academy of Sciences, Prague

Air pollution has been notoriously known problem connected with human activities mainly in industrial countries. Solution of this problem has been sought for decades. It has already been proven that this process takes place in the atmospheric boundary layer (ABL) and that it is a very complicated and synergic problem. The methods of mathematical and physical modelling are used in its solution, accompanied by theoretically and financially demanding experiments serving for specific configuration solution or for validation of methods used in modelling.

The physical modelling is based on principles of analogy, especially an analogy between flow in ABL and flow in boundary layer modelled in special wind tunnel that meets dynamical, thermal and geometrical similarity criteria. Even here however, there is no universal method, so methods of approximate simulation that solve task classes are deduced. In case of disaster, accidental gas release or fire accompanied by gas escape, the situation is very complicated. The gas usually releases inside the industrial area, among the buildings or obstacles, often in topographically complicated terrain. Aim of the paper is to present the method of physical modelling for simulation of dispersion of gas in small scale (hundreds of metres) inside the urban area and describe results of measuring pollutions concentration in a specific accident situation around the train station.

Keywords: air pollution, atmospheric boundary layer, modelling, validation.

Introduction

Expansion of human society has a significant impact on the condition of the environment. Significant influence is visible in towns and surrounding countryside. The atmosphere is one of the most endangered spheres. People in city agglomerations are threatened with air pollution from traffic, house heating and industry. One of the most significant cases of environmental pollution is an accident with an escape of harmful substances. The possible source of such escape is a device that contains bigger amount of harmful gas or contains substance that can release gas in appropriate conditions.

For example: an ice-hockey arena with cooling system full of ammonia, containers with liquid gas (chlorine, propane-butane…) and gases developed in fire of plastic. Another activity that can participate in atmospheric pollution is an intentional fault. More and more frequent attacks of radical groups are aiming to cause as large impact as possible.

Physical modelling

Essentially all the above-mentioned activities of man are influenced by atmospheric motions from ground up to a height of thousand meters. Processes in this layer, so called the Atmospheric Boundary Layer (ABL) are complicated by the combined influences of the Earth's rotation, buoyancy forces, surface drag forces, and the geometry of topographic features. It is extremely difficult to solve this synergetic problem analytically and experiments in situ are expensive and give only particular results. The main source of information for solving of environmental and wind engineering problems is mathematical modelling and a laboratory simulation of the ABL in specially designed wind tunnels. The basic physical model is a boundary layer formed over the floor of a wind-tunnel working section. The general requirements for geometric, dynamics and thermical similarity, obtained by inspectional analysis are, e. g.: undistorted scaling of geometry, equal Reynolds number Re, equal Prandtl number Pr, equal Richardson number Ri, equal Eckert number Ec, surface-boundary-conditions similarity, similarity of the approach-flow characteristics has to be fulfilled depending on accuracy of demanded information. However, the requirements cannot be satisfied simultaneously in existing facilities and a partial or approximate simulation for particular application has been worked out. E.g.:

- Monin, Obukhov's theory [4] is applied for micro-scale flows with horizontal dimension $L_0 \sim (10^{-1} - 10)$ m, can be used for urban canopy.
- Laminar-turbulent similarity [1] is used for stratified meso-scale flow of dimension $L_0 \sim (2\ 10^2 - 2 \cdot 10^6)$ m.
- Reynolds' number independence [2] is used for micro-scale flow of dimension $L_0 \sim (10 - 2\ 10^2)$ m over rough surface or over buildings and street canopy, this method was used in our study.

Method of approximate simulation that is necessary for simulation of processes above the urban buildings or processes among the urban buildings was deduced for modelling of flow and diffusion in the near surrounding of source located among the urban buildings. For the simulation of city buildings against the flow in investigated terrain, we assume that in front of investigated model there are large enough, horizontally homogenic suburban buildings. Then it is possible to simulate such buildings as flow above the rough surface geometrically similar to prototype [5]. It means that model boundary layer created on the wall of wind tunnel is proportionally similar to appropriate atmospheric boundary layer. For indifferent atmospheric layering the velocity profile is defined by a logarithmic profile

$$U(z) = \frac{u^*}{k} \cdot \ln\left[\frac{z-d}{z_o}\right]$$

where u* is frictional velocity (dynamic velocity), k = 0.4 is von Karman's constant, z_o is frictional height (aero dynamical roughness), d is shift, U is mean velocity and z is vertical coordinate.

Near surroundings of source is performed as a model of location in a given scale.

Experimental facilities

A few dozens of special wind tunnels for simulation have been built all over the world. The boundary layer wind tunnel at VZLU (Aeronautical Research and Test Institute) in Prague is designed as a fan driven open-circuit facility, see Fig. 1. There is the test section of 1.85 m x 1.55 m cross section and a length of 13.65 m. The tunnel inlet is formed by circuit elements inside the suction part with 35 m^2 screens. It follows a corner with 24 vanes. There is working section of the length 2 m with glass sidewalls. A 55 kW axial blower at the exit drives the tunnel. The velocity at the working section is within interval (0.1; 15) $m \cdot s^{-1}$.

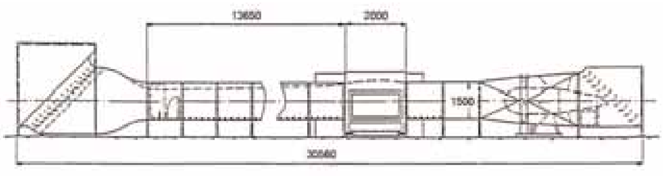

Fig. 1 — Boundary Layer Wind Tunnel (BLWT) at the VZLU

To verify the characteristics above the urban buildings, the characteristics of flow at the entrance into the test section were measured. Measurements were conducted by hot wire anemometer. From measured values vertical profiles of mean velocity, profiles of turbulence intensity and profiles of Reynolds stress were evaluated — see Fig 2.

All profiles were measured for velocity 4 $m \cdot s^{-1}$ at the working section axis. Measurements are conducted in three positions, in tunnel-axis and 500 mm right and left; profiles measured are in Fig. 2. From the values measured, the value of parameter of roughness $z_0 \approx 0.54$ mm and friction velocity $u^* \approx 0.236$ $m \cdot s^{-1}$ were calculated. These values correspond with values in full-scale $z_0 \approx 0.2$ m that e.g. according to Snyder method (Snyder 1981) correspond with suburban terrain. Fig. 2 shows logarithmic part of profile of mean velocity that corresponds with indifferent stratification atmosphere. Intensity of turbulence has also expected character with maximum by the surface and with growing height decreases up to values of about 6% over boundary layer. Profile of Reynolds stress shows area of constant Reynolds stress in range 0-220 mm that again corresponds with modelled boundary layer.

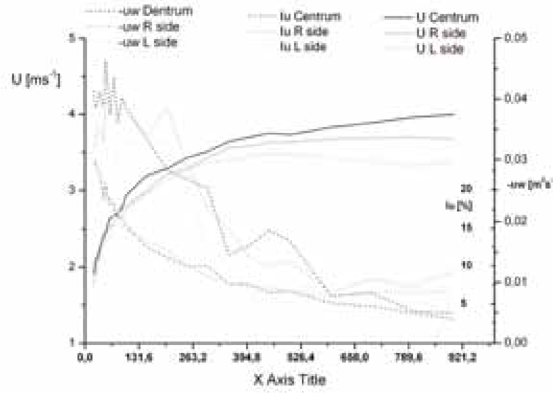

Fig. 2 — Properties of boundary layer

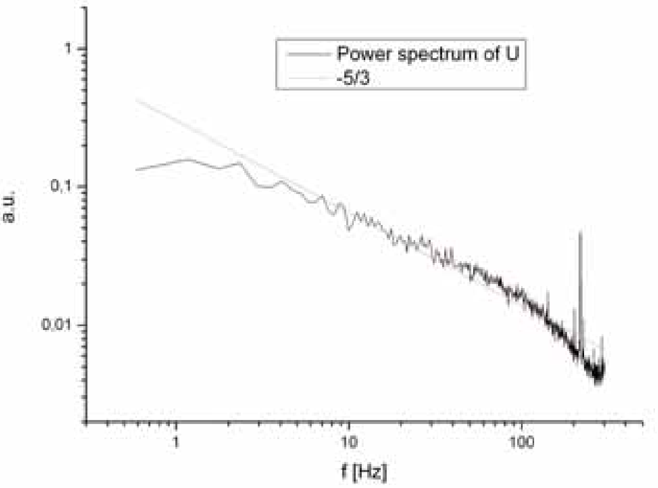

Fig. 3 — Power spectrum of velocity

Spectrum was evaluated from velocity measurement in height 150mm above the surface in tunnel-axis. Spectrum was determined as means of multiple Fast Fourier Transformations (FFT). The obtained data were divided into several blocks, afterwards FFT for all blocks ware calculated and results were calculated as a mean. Spectrum obtained shows agreement with rule -5/3 in range 2-200 Hz, see Fig. 3.

Model scale was deduced from the shape of autocorrelation curve (ACF) as integral length evaluated from area bellow centred ACF. The limits for integration in calculation of integral length are from zero to first zero crossing. The in-flow corresponded with terrain of medium roughness z_{od}=0.220 m (index d denotes the value in full scale) in conditions of thermal and energetic equilibrium in evaluated scale 1:380 [3].

An orifice of 3 mm diameter on the ground level with tracer was used for simulation of accident with gas leakage. Ethane was used for the simulation of leakage of non-buoyancy gas. Specimens were collected by rake probe and peristaltic pump that into flame ionisation detector (FID).

Concentrations obtained this way have to be transformed into the dimensionless concentration C* [6], that is not dependent on model parameters and enables us to perform estimation of gas dispersion in full scale. C* can be defined as

$$C^* = \frac{C\left[\frac{kg}{m^3}\right] U\left[\frac{m}{s}\right] \cdot L^2[m]}{Q\left[\frac{kg}{s}\right]}$$

where C is the concentration measured on model, L is the characteristic dimension — the height of the train station building, U is the characteristic velocity — the velocity in the height L and Q is the source yield.

Results

The method of independence of Re was used for the modelling of emission dispersion on a train. The model of the train station and nearby buildings in 1:380 scale was manufactured see Figs. 4 and 5. The diameter of model is 1,5m that corresponds to a circle with a diameter of 570m in full scale.

Fig. 4 — Photo of train station

The source of emissions was approximately at the entrance of train station building. Outflow gas volume was 0,4 slpm (standard liters per minute), the lowest adjustable on flowmeter. Measurements of concentrations are performed in the plane perpendicular with BWLT axis, 600mm behind the emissions source and in horizontal layer behind the source, 2m above ground level. Horizontally oriented rake probe that can guarantee collection from up to 4 collection places was used for concentration measurement, see Figs. 6 and 7.

Comparing the model topography and measured profiles, the influence on measurement results is clearly visible. It concerns swerve of maximum value of horizontal concentration profile along the of long buildings that form direction of wind. Another influence of this topology is dividing of concentration peak that is probably caused by presence of square object 100m in full scale in front of collection probe.

Fig. 6 shows the isoconcentration lines in the plane of collections evaluated from the measured horizontal profiles.

In Fig. 8 there is the concentration profile printed on the photo of the train station in full scale. The source is marked by red circle; the wind blow from the left side to the right side in parallel direction with the horizontal axes of the picture.

Conclusions

Following practical example shows application of obtained results in dimensionless quantities. In case of escape of CO nearby the entrance of railway station building, e.g. as a result of fire, it is necessary to know following data: velocity and direction of wind in previously stated reference point, e.g. on the rooftop of the building; prior defined reference height, for example height of building; source yield of emission; dimensionless concentrations measured and calculated by method of physical modelling

Using input data U=1 ms-1, C*=0, 3 - maximum measured, approx. 300m behind the source in the wind direction in height approx. 3 m, l=26,6 m — height of building, Q=1 kgs^{-1} of CO, concentration 400 μgm^{-3} was obtained by all above-mentioned values simply multiplied by mentioned equal.

Problem of an accident was studied. Method of physical modelling was applied on complex topological terrain. Measurements of diffusion was performed and the influence of specific topology of environment on gas dispersion was shown. Calculations that show possible application of physical modelling in estimation of pollution as a consequence of escape of harmful gas into the atmosphere were performed.

Acknowledgement

The work was supported by the CR Ministry of Education, Youth and Physical Training *External Aerodynamics Development* research project (MSM 0001066901) and the Grant Agency of the Czech Republic (GACR 205/04/0311).

Editorial note: Further numbered illustrations to this article mentioned in text are printed in colour on back cover page.

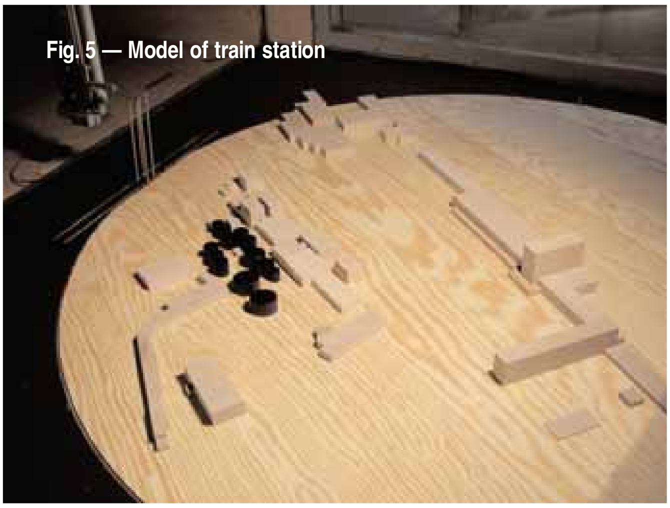

Fig. 5 — Model of train station

References:

[1] Cermak J. E.(1976): *Aerodynamics of Buldings*; Annual Review of Fluid mechanics, 8, p. 75

[2] Janour, Z., Dittert, F. Severa, M. *et al* (1999): *Air-Pollution Wind Tunnel Modelling*; International Conf. Problems in Fluid Mechanics and Hydrology, pp. 490-497

[3] Jirsak, M., Ulman, R. (2001): *Boundary layer simulation and its lower velocity limit*; Proc. 3rd European African Conf. On Wind Eng., Eindhoven University, pp. 237-240

[4] Monin A. S., Obukhov A. S. (1953): *Dimensionless characteristics of turbulence in the atmospheric surface layer*; Doklady AN SSSR 93, p. 223

[5] Snyder, W. H. Dudeline, (1981): *For Fluid Modelling of Atmospherics Diffusion, Enviromental Protection Agency*; Research Triangle Park, NC 27711, 1981 Report No. 600/8-81-009

[6] Ulman, R., Janour, Z., Sedenkova, H., Drbohlav, J.: *The physical modelling of gas dispersion in topographically complicated terrain*; Proceedings EACWE 4, Praha 11.-15.7.2005, pp. 328, 329, ISBN 80-86246-26-4

TITUS MPP Facility — Tool for the Crystal Growth and Solidification on Board the International Space Station (ISS)

Some colour illustrations to the article published on pages 16-21.

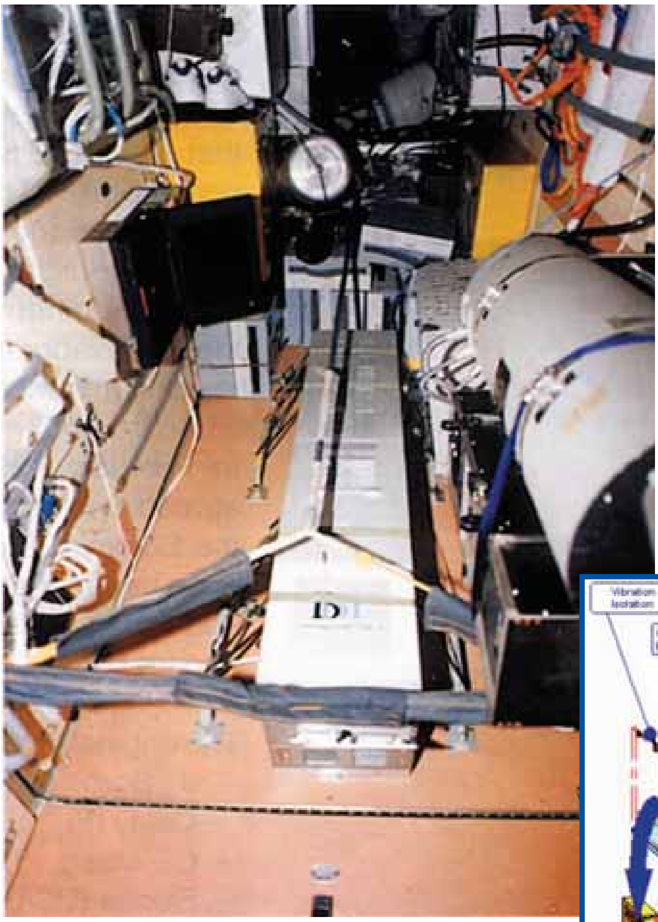

Fig. 5 (Above) — TITUS and CSK-1C space facilities on board the MIR space station. Project MIR ‘99 - PERSEUS [Photo CNES, France]

Fig. 6 (Below) — Artist's view of the ”TITUS MPP Facility“

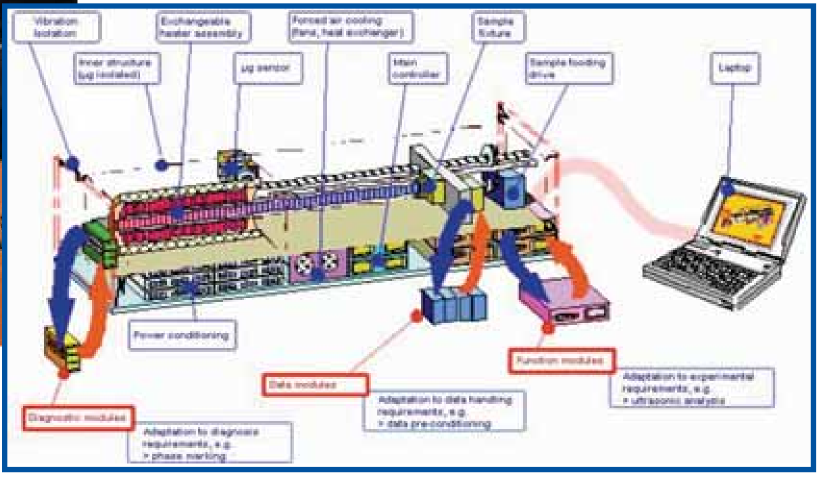

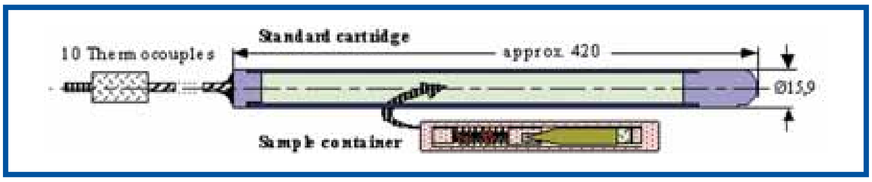

Fig. 7 — Standard experiment cartridge with a sample container — basic configuration

Fig. 9 — TITUS MPP - Bread-board model BM-2 (furnace module)

Harmful Gas Dispersion around the Train Station

Further colour illustrations to the article published on pages 34-36.

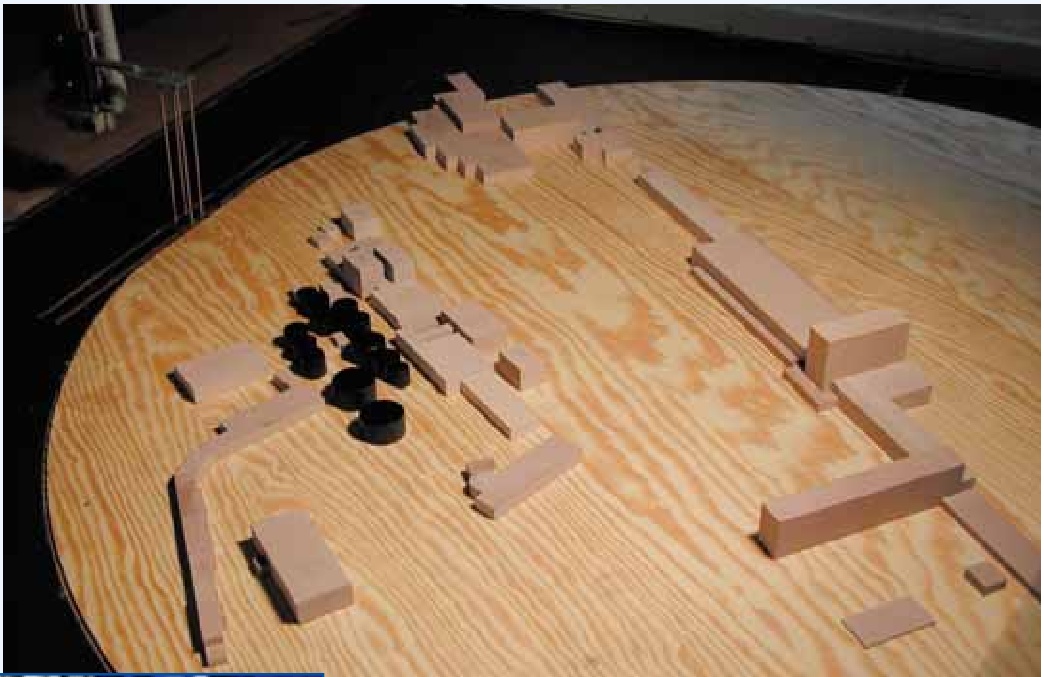

Fig. 5 (above) — Model of the train station

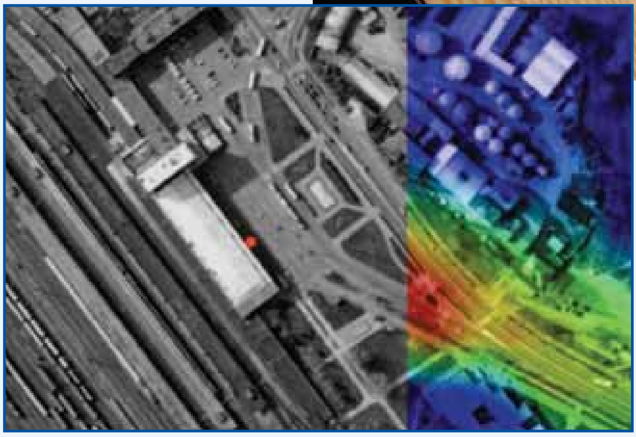

Fig. 8 (left) — Dimensionless concentration behind the source

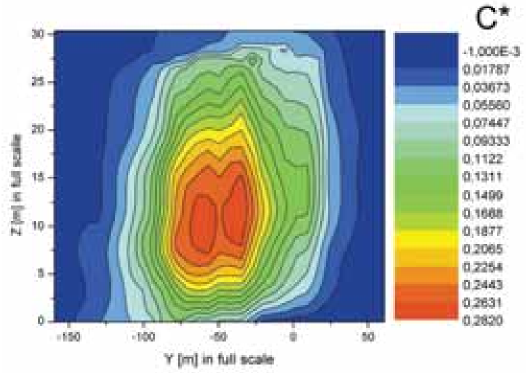

Fig. 6 — Vertical profile of concentrations

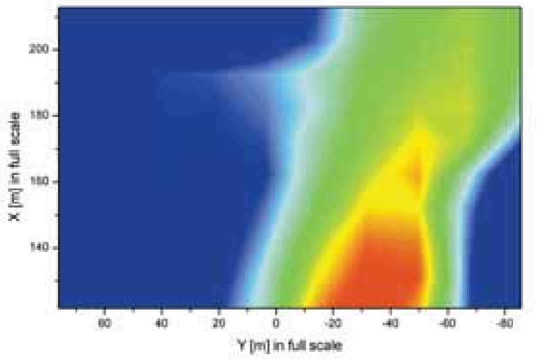

Fig. 7 — Horizontal profile of concentrations